



TITLE:

Theoretical Analysis of Supersonic Gas-Particle Two-Phase Flow and Its Application to Relatively Complicated Flow Fields

AUTHOR(S):

HATTA, Natsuo; FUJIMOTO, Hitoshi; ISHII, Ryuji;
KOKADO, Jun-ichi

CITATION:

HATTA, Natsuo ...[et al]. Theoretical Analysis of Supersonic Gas-Particle Two-Phase Flow and Its Application to Relatively Complicated Flow Fields. *Memoirs of the Faculty of Engineering, Kyoto University* 1990, 52(3): 115-185

ISSUE DATE:

1990-07-31

URL:

<http://hdl.handle.net/2433/281418>

RIGHT:

Theoretical Analysis of Supersonic Gas-Particle Two-Phase Flow and Its Application to Relatively Complicated Flow Fields

by

Natsuo HATTA*, Hitoshi FUJIMOTO*, Ryuji ISHII**
and Jun-ichi KOKADO***

(Received February 20, 1990)

Abstract

This paper describes supersonic flows of a gas-particle two-phase mixture in considerably complicated situations. For the flow field of gas-particle mixtures such that the gas-phase and the particle-phase interact with each other, the model is constructed by incorporating the particle-trajectory method into the system of gas-phase equations in the two-fluid model. First, the one-phase and two-phase flows of round underexpanded jets exhausted from a sonic nozzle are investigated in detail. The one-phase results are compared with the experimental ones in order to confirm whether the present scheme is reliable or otherwise. For the two-phase results, the particles with the same velocity and temperature as those of the gas-phase are injected at the nozzle exit plane, and the effect of the presence of the particles on the flow field is examined by comparing these two-phase results with the one-phase ones. Second, the results of the numerical experiments in which underexpanded sonic round jets impinge on a flat plate normal to the jet axis are presented and analyzed for both the one-phase and two-phase cases. For the one-phase flow, periodic unstable oscillations have been found to give fairly good agreement with the experimental results. Third, supersonic gas-particle two-phase flows around a sphere are simulated in view of the numerical experiments. The instability in the particle motion near the stagnation region in the shock layer is discussed in detail. A few new findings are also described throughout the present paper.

1. Introduction

A number of processes in iron and steelmaking industries positively introduce the utilization of the two-phase or multi-phase flows. Therefore, we have investigated the numerical analyses of the gas-particle mixture flows in a nozzle

* Dept. of Mineral Science and Technology, Faculty of Eng., Kyoto Univ., Kyoto 606

** Dept. of Aeronautical Eng., Faculty of Eng., Kyoto Univ., Kyoto 606

*** Niihama College of Technology, Niihama 792

for a few years, and obtained some new findings. First, a system of equations governing the steady quasi-one-dimensional nozzle flow of a gas-particle mixture, described by Zucrow and Hoffman¹⁾, has been extended to the case where a continuous distribution of particle size is present. Then, we have solved the system of modified equations in view of the numerical experiments and demonstrated how the phase non-equilibrium phenomena are observed in the subsonic nozzle flows²⁾. Therein, the case has been treated where a gas containing a suspended condensed liquid-phase is initially stored in a considerably large reservoir, and the gas-particle mixture directly flows through a nozzle. At the reservoir the gas velocity as well as the particle velocity is regarded as zero. That is to say, this fact corresponds to the condition that the sectional area of the nozzle is infinite at the nozzle entrance. Hence, a numerical procedure such that all the particles are in velocity and thermal equilibrium with the gas-phase only near the reservoir has been introduced to the numerical experiments. In short, it follows that the non-equilibrium flow is treated as a perturbation from an equilibrium reference flow. Here, one of the most important problems is that the pressure at the reservoir is not permitted to be so high that the gas velocity is beyond the sonic state, because the system of equations described in Ref. (2) is singular in the transonic region.

Hence, we have rewritten an equation to evaluate the gas velocity into another type of equation so that it may cover the whole gas velocity from the subsonic to the supersonic velocities through the throat of a converging-diverging nozzle³⁾. That is, the equation has been rewritten in the form including the term of pressure gradient along the whole nozzle axis instead of the term of the varied nozzle cross-sectional area along the axis. Here, we note that the governing equations to determine all of the flow properties, except the aforementioned gas velocity, are the same as the previous case (see Ref. 2). Therefore, it is necessary to give the pressure gradient along the axis as one known parameter. Thereby, the nozzle configuration can uniquely be determined in consistency with the given pressure gradient.

Thereafter, for the prescribed nozzle configuration also, the numerical analysis of the supersonic nozzle flows of the two-phase gas-particle mixtures has been investigated from a practical point of view⁴⁾. In this situation, the specified area method is employed upstream as well as downstream from the transonic region, and the specified pressure method is employed in the transonic region. At a glance, it seems that this is not tedious in the numerical treatment. However, the case can occur where the pressure gradient to be assumed in the transonic region is not suitable to the perturbation from the results evaluated by

the specified pressure method, and an unfortunate gap appears between the calculated nozzle sectional area and the previously prescribed area. Therefore, a reasonable numerical model to avoid such a problem has been proposed from an analytical point of view.

As has been mentioned above, a theoretical or analytical procedure to evaluate all of the flow properties of the gas-particle mixtures in a nozzle has been nearly completed, although the flow is limited to the quasi-one-dimensional system.

Next, what is considered to be more important is to understand the flow pattern of the gas-particle two-phase flows exhausted from a nozzle. That is, the numerical analysis of the gas-particle two-phase flows, not only in a nozzle but also in a free jet region, is of great technical importance for various engineering applications. However, the numerical analysis of this problem is difficult as regards a few aspects. First, a multi-dimensional system such as two- or three-dimensional, cylindrical coordinate ones must be adopted for the computational domain. Therefore, a long computational time is required. Second, the gas-phase and the particle-phase are treated not as the same media, but as different media. Third, there is an ambiguity in the magnitude of the computational domain as well as the selection of the boundary conditions.

This paper is concerned with a numerical analysis of gas-particle two-phase flows in relatively complicated flow fields.

Consider a particle located at an upstream point of the flow field of a gas-phase, whose initial states are perfectly known. There is a technique to follow the later motion of the particle, which is commonly called the particle trajectory method. The numerical model for dilute gas-particle flows is constructed by incorporating the above trajectory method into the system of gas-phase equations in the two-fluid model. Here, we consider gas-particle mixtures such that the gas-phase and particle-phase interact with each other.

In general, even when one can regard the particle cloud in a flowing medium as very dilute, it is necessary to take the average values over an appropriate volume in order to define properties such as velocity, temperature and density of the particle cloud. In this sense, the particle velocity is generally specified by two quantities, the mean velocity, \bar{q}_p , and the fluctuating velocity, Δq_p . For the motion of the particle-phase, one of the most important physical values is the mean square of the measured value of the fluctuation denoted by $\langle \Delta q_p^2 \rangle$. The product of $\langle \Delta q_p^2 \rangle$ and the particle-phase density just corresponds to the pressure for the gas-phase case from the point of view of the behaviour of the particle-phase. In order to see a global view of the motion of the particle cloud, we

define a parameter described by $|\bar{q}_p|/\langle\Delta q_p^2\rangle^{1/2}$. The particle-trajectory method may be accepted on the premise that the motion of each particle is perfectly deterministic. Thus, when the condition that $|\bar{q}_p|/\langle\Delta q_p^2\rangle^{1/2}\rightarrow\infty$ is satisfied, the particle-trajectory method can be applied in a natural as well as an appropriate fashion. We now consider a characteristic of the flow field of the particle-phase on the above condition. The fact that the fluctuation of the particle velocity is negligibly small leads to the situation that in a dilute particle cloud there is no analog to pressure, and the particle information is not transmitted by particle-particle collisions but only along particle trajectories. That is to say, an important difference between a continuum and a dilute particle cloud is the mechanism for information transfer. In a continuum, information is transmitted by pressure waves, namely through molecular (actually particle-particle) interaction.

Next, we will consider the above condition from another angle. It is well-known in the gasdynamics that the mean square of velocity in a random motion of gas molecule gives the temperature of the gas phase, and in turn the root of the temperature is proportional to the speed of sound. Assuming the similarity of such a fact, the condition that $|\bar{q}_p|/\langle\Delta q_p^2\rangle^{1/2}\rightarrow\infty$ suggests that the particle cloud is highly supersonic in a dilute gas-particle flow, and therefore is highly compressible. In fact, many dilute gas-particle flows are observed to be very similar to the supersonic flow of the gas phase. That is, in the flow fields of mixtures, the region where particles are not present at all, or on the contrary, the region where they extraordinarily aggregate themselves is formed in a very easy way. From such a point of view, it is important to point out that the particle cloud may be regarded as a continuum even in the limit of infinite dilution⁵⁾.

In short, we may consider that the flow field of the particle-phase has two characteristics contradictory to each other. One is a discrete feature due to the fact that there is no analog to pressure (or pressure waves). The other is a continuum feature owing to the fact that the particle flow field is highly compressible.

Again, for the case where velocity fluctuations of the particle cloud are negligible or not present in the flow field at all, the particle-phase properties can easily be evaluated by following some appropriate and representative particles along each particle trajectory in a Lagrangian fashion.

Once again, we will consider the diluteness of the particle-phase from a quantitative point of view. It is commonly accepted that the material density $\bar{\rho}_{mp}$ of an usual solid or liquid particle is larger by a magnitude of order of 10^3 than that of a gas $\bar{\rho}$. We define the ratio, ν , of the mass of the particle-phase to that

of the gas-phase per unit volume as $\nu = \bar{n}_p \bar{m}_p / (1 - \varepsilon_p) \bar{\rho} = \varepsilon_p \bar{\rho}_{mp} / (1 - \varepsilon_p) \bar{\rho} \simeq \varepsilon_p \bar{\rho}_{mp} / \bar{\rho}$, where \bar{n}_p , \bar{m}_p and ε_p denote the number density, the mass of a particle of \bar{r}_p in radius and the volume fraction occupied by the particle-phase per unit volume, respectively. Thus, we have $\varepsilon_p = \nu \bar{\rho} / \bar{\rho}_{mp}$. When a particle of \bar{r}_p is injected into a uniform space involving the particle cloud of the mean particle spacing \bar{l}_p , the particle mean free path $\bar{\lambda}_p$ travelled between particle-particle collisions is expressed by the order of $\bar{l}_p / \varepsilon_p^{2/3}$. Thus, $\bar{\lambda}_p / \bar{L} \approx (\bar{l}_p / \bar{L}) / \varepsilon_p^{2/3}$, where \bar{L} indicates a characteristic length of the flow field. Therefore, if $\bar{l}_p / \bar{L} = O(\varepsilon_p^{2/3})$, then $\bar{\lambda}_p / \bar{L} = O(1)$. In this case, the gas-particle mixture may be regarded as dilute, and the direct collisions between particles can be neglected. For usual dusty gas flows, the order of ν is unity ($\nu = O(1)$). Therefore, $\varepsilon_p = O(10^{-3})$. That is to say, if $\nu = O(1)$, $\bar{l}_p / \bar{L} = O(10^{-2})$ is a sufficient condition for the particle-phase to be dilute, and the behaviour of the particle-phase can uniquely be determined.

As mentioned above, it can often be observed that the particle cloud breaks up into a large number of subclouds and also particle-free regions appear in the flow field. When a flow is highly unsteady, disintegration of a particle cloud commonly produces some small subclouds. These subclouds can in turn coalesce or collide with each other in some different flow regions. Here, we should like to stress that the collisions between particle subclouds do not always result in the direct collision between particles in the clouds. According to our above discussion, particle-particle collisions are negligible even when collisions between particle subclouds occur, if $\nu = O(1)$ and hence ε_p is negligibly small.

In the present model, the whole particle cloud is divided into a large number of small subclouds. It is assumed that all the particles belonging to each subcloud have the same velocity and temperature. The particle flow field is solved by selecting an appropriate and representative particle in each subcloud and by following the properties of the particle along the particle trajectory. On estimating the momentum and energy transfer rates from the particle-phase to the gas-phase, the contributions from the clouds take average values over a volume. The cross-sections of the subclouds and the averaging volume are determined so that the conditions that $\bar{l}_p^2 \ll \Delta \bar{S}_p \ll \bar{S}_p \ll \bar{L}^2$ are satisfied, where $\Delta \bar{S}_p$ and \bar{S}_p are the cross-sectional areas of the clouds and the averaging volume, respectively.

In the present paper, on the above premises, we wish to treat some significant and attractive problems concerning the flow fields of two-phase mixtures from an analytical standpoint.

First, the gas-phase jet flows exhausted from a sonic nozzle are investigated in detail. The results so obtained are compared with the experimental ones in

order to confirm whether the present scheme is reliable or otherwise.

Successively, the particles with the same velocity as that of the gas-phase are injected at the nozzle exit, and the effect of the presence of particles on the flow field of the gas-phase is investigated by comparing these two-phase results with those of the previous one-phase ones.

Also, an unstable flow field of a gas-only jet impinging on a disk whose diameter is taken to be equal to that of the nozzle exit is numerically investigated. Next, in the jet flows the particles are injected into the gas-jet at fixed points on the nozzle exit plane. The particle cloud is divided into two groups; one of which is the particle cloud impinging on the disk and elastically reflecting from it. The other is the particle cloud passing around the outer side of disk. The numerical results obtained in such a situation are described, focusing upon the instability of the flow field of the gas-phase and particle-phase before and behind the disk.

Furthermore, a situation is treated where a two-phase mixture flowing in an equilibrium state approaches a semi-spherical body and interacts with it. Similarly to the disk case, the particle cloud is divided into the particle group impinging on the body surface and elastically reflecting from it, and into the group passing through without any impingement on the sphere. Such supersonic gas-particle two-phase flows around the spherical body are simulated, and the effects of the presence of particles on the flow field in the shock layer are inspected by comparing the two-phase results with the single-phase ones in detail.

2. System of governing equations

The theoretical flow model for dilute gas-particle flows is constructed in a two-dimensional (\bar{x}, \bar{y}) coordinate system on several usual assumptions, although a few important assumptions among them introduced into the present analysis have been mentioned in the previous introduction. Again, we wish to address them with other important assumptions. First, no phase transformations such as evaporation, condensation and sublimation take place. Second, the mass flow rate for both gas- and particle-phases is conserved in a system treated here. But the particles occupy negligible volume, that is, the ratio of the density of the gas-phase to that of the particle-phase is negligibly slight. Third, the mean particle spacing is sufficiently smaller than the smallest scale of the flow field ($\bar{l}_p/\bar{L} = O(\epsilon_p^{2/3})$). Fourth, the motion of a gas carrying suspended particles obeys the two-dimensional Euler equations. Namely, the gas-phase is regarded as inviscid,

apart from the drag force exerted by all of the particles on the gas. Fifth, all of the particles are spherical in shape with a uniform diameter, incompressible and do not interact with each other. Sixth, the momentum and heat transfers from the particle-phase to the gas-phase are taken into consideration. Seventh, there is no internal temperature distribution in the radial direction of particles, and the particles, as well as the gas, have a constant specific heat.

On the above premises, the system of equations governing two-phase gas-particle mixture flows will be derived in a separate form for the gas-phase and the particle-phase. Previously, we wish to state that the dimensional quantities are denoted by the overbar, and no overbar denotes the dimensionless quantities throughout the present paper. Again, the subscripts p and r denote particles and reference conditions, respectively.

2.1 Particle-phase

A particle cloud which is fed at an upstream boundary at a certain time t^* is divided into a large number of subclouds with an appropriate cross-sectional area. Here, let it be assumed that the initial state of each subcloud is perfectly known. A particle located at the center of a subcloud will be called the representative particle, and the particle is numbered by subscripts k ($k=1, 2, 3, \dots$). Denoting the coordinate, velocity and temperature of the k -th representative particle at a given time $t(>t^*)$ by $(\bar{x}_{pk}(t), \bar{y}_{pk}(t))$, $(\bar{u}_{pk}(t), \bar{v}_{pk}(t))$ and $\bar{T}_{pk}(t)$, respectively, we have the system of equations of motion obeying the Newton law in the following form:

$$\frac{d\bar{x}_p}{dt} = \bar{u}_p \quad (1)$$

$$\frac{d\bar{y}_p}{dt} = \bar{v}_p \quad (2)$$

$$\frac{d\bar{u}_p}{dt} = \bar{A}_p(\bar{u} - \bar{u}_p) \quad (3)$$

$$\frac{d\bar{v}_p}{dt} = \bar{A}_p(\bar{v} - \bar{v}_p) \quad (4)$$

Again, a particle energy equation can be derived by taking it into account that the heat transfer between the gas and the particle affects only the particle enthalpy \bar{h}_p through the surface area of the particle ($= 4\pi\bar{r}_p^2$) in the form of

$$\frac{d\bar{h}_p}{dt} = \bar{B}_p(\bar{T} - \bar{T}_p) \quad (5)$$

in which $(\bar{x}_{pk}(t), \bar{y}_{pk}(t))$, $(\bar{u}_{pk}(t), \bar{v}_{pk}(t))$ and $\bar{T}_{pk}(t)$ are abbreviated simply to (\bar{x}_p, \bar{y}_p) , (\bar{u}_p, \bar{v}_p) and \bar{T}_p in Eqs. (1) to (5), respectively. Also, \bar{u} , \bar{v} and \bar{T} indicate the velocity components in the \bar{x} - and \bar{y} -directions and the temperature of the gas-phase at (\bar{x}_p, \bar{y}_p) , respectively. \bar{A}_p and \bar{B}_p are given by

$$\bar{A}_p = \frac{9}{2} \frac{\bar{\mu} f_p}{\bar{\rho}_{mp} \bar{r}_p^2} \quad \text{and} \quad \bar{B}_p = \frac{3\bar{\mu} g_p \bar{C}_{pg}}{\bar{\rho}_{mp} \bar{r}_p^2 Pr} \quad (6)$$

respectively. Here, Pr is the Prandtl number of the gas-phase. The parameters, f_p and g_p are defined by

$$f_p = \frac{C_D}{C_{D, Stokes}} \quad \text{and} \quad g_p = \frac{Nu}{Nu_{Stokes}} \quad (7)$$

in which C_D and Nu represent the drag coefficient and the Nusselt number ($Nu \equiv \bar{a}(2\bar{r}_p)/\bar{\kappa}$, \bar{a} ; the heat transfer coefficient, $\bar{\kappa}$; the thermal conductivity of the gas), respectively. The subscript, *Stokes*, denotes the Stokes flow regime (i.e., $Re < 1$, Re ; the particle Reynolds number). \bar{C}_{pg} is the specific heat of the gas-phase at a constant pressure. Also, the gas viscosity $\bar{\mu}$ is given by

$$\bar{\mu} = \bar{\mu}_r \left(\frac{\bar{T}}{\bar{T}_r} \right)^\delta \quad (8)$$

where the exponent δ is a constant.

In general, Eqs. (1) to (5) are simply rewritten in the following vector form of

$$\frac{d\bar{\mathbf{E}}_{pk}}{dt} = \bar{\mathbf{I}}_{pk} \quad (k=1, 2, 3, \dots) \quad (9)$$

in which

$$\bar{\mathbf{E}}_p = \begin{bmatrix} \bar{x}_p \\ \bar{y}_p \\ \bar{u}_p \\ \bar{v}_p \\ \bar{h}_p \end{bmatrix} \quad \text{and} \quad \bar{\mathbf{I}}_p = \begin{bmatrix} \bar{u}_p \\ \bar{v}_p \\ \bar{A}_p(\bar{u} - \bar{u}_p) \\ \bar{A}_p(\bar{v} - \bar{v}_p) \\ \bar{B}_p(\bar{T} - \bar{T}_p) \end{bmatrix} \quad (10)$$

One should bear in mind that the above equations are applicable to following the behaviour of a particle of \bar{r}_p in radius. Therefore, in principle, the particle flow field should be solved by following all the particles using the above equations. However, there are too many particles in the flow field to do this.

Then we consider a large but tractable number of small subclouds. Now, one remaining task is how to evaluate the numerical treatment of the particle number \bar{N}_{pk} contained in the k -th subcloud. In practice, when a cloud is injected into a flow field at a time \bar{t}^\dagger at a point $(\bar{x}_{pk}(\bar{t}^\dagger), \bar{y}_{pk}(\bar{t}^\dagger))$ ($k=1, 2, 3, \dots$), \bar{N}_{pk} remains unvariable on a two-dimensional computational plane at a given time \bar{t} ($>\bar{t}^\dagger$) at a position $(\bar{x}_{pk}(\bar{t}), \bar{y}_{pk}(\bar{t}))$ for the case where the flow system is selected in the form of the Cartesian coordinate. However, the case of the axisymmetric flow system must be different from the foregoing case. The particle cloud in the physical space forms a ring cloud when the flow is axisymmetric. So the number of particles contained in the k -th subcloud is given by $2\pi\bar{y}_{pk}\bar{N}_{pk}$. Thus, we have

$$2\pi\bar{y}_{pk}\bar{N}_{pk} = 2\pi\bar{y}_{pk}^\dagger\bar{N}_{pk}^\dagger$$

or

$$\bar{N}_{pk} = (\bar{y}_{pk}^\dagger/\bar{y}_{pk})\bar{N}_{pk}^\dagger \quad (11)$$

where the cross denotes the conditions of the particles in the k -th subcloud at the injecting point.

2.2 Gas-phase

The Euler equations for the two-dimensional (or axisymmetric) inviscid flow consist of the energy equation, the continuity equation and the momentum equation. For the sake of simplicity, we first consider the single-phase (gas-only) flow. The total energy, \bar{e} , per unit volume of the gas can be represented by the addition of the internal energy, $\bar{\rho}\bar{t}$ ($\bar{t}=\bar{C}_{vg}\bar{T}$, \bar{C}_{vg} ; specific heat at constant volume), to the kinetic energy as

$$\begin{aligned} \bar{e} &= \bar{\rho}\bar{t} + \frac{\bar{\rho}}{2}(\bar{u}^2 + \bar{v}^2) = \bar{\rho}\bar{C}_{vg}\bar{T} + \frac{\bar{\rho}}{2}(\bar{u}^2 + \bar{v}^2) \\ &= \frac{\bar{p}}{\gamma-1} + \frac{\bar{\rho}}{2}(\bar{u}^2 + \bar{v}^2) \end{aligned} \quad (12)$$

in which \bar{p} is the pressure of the gas.

So that, the energy equation can be written on the basis of the conservation law by

$$\frac{\partial \bar{e}}{\partial \bar{t}} + \frac{\partial}{\partial \bar{x}}(\bar{e}\bar{u}) + \frac{\partial}{\partial \bar{y}}(\bar{e}\bar{v}) + \frac{\partial}{\partial \bar{x}}(\bar{p}\bar{u}) + \frac{\partial}{\partial \bar{y}}(\bar{p}\bar{v}) + j\frac{\bar{v}}{\bar{y}}(\bar{e} + \bar{p}) = 0$$

or

$$\frac{\partial \bar{e}}{\partial t} + \frac{\partial}{\partial x} \{\bar{u}(\bar{e} + \bar{p})\} + \frac{\partial}{\partial y} \{\bar{v}(\bar{e} + \bar{p})\} + j \frac{\bar{v}}{y} (\bar{e} + \bar{p}) = 0 \quad (13)$$

in which $j=1$ if the flow system is axisymmetric. If otherwise, $j=0$ (for the two-dimensional Cartesian coordinate system).

Next, the continuity equation can be expressed in the form of

$$\frac{\partial \bar{\rho}}{\partial t} + \frac{\partial}{\partial x} (\bar{\rho} \bar{u}) + \frac{\partial}{\partial y} (\bar{\rho} \bar{v}) + j \frac{\bar{\rho} \bar{v}}{y} = 0 \quad (14)$$

Again, the momentum equations are given by

$$\frac{\partial}{\partial t} (\bar{\rho} \bar{u}) + \frac{\partial}{\partial x} (\bar{\rho} \bar{u}^2) + \frac{\partial \bar{p}}{\partial x} + \frac{\partial}{\partial y} (\bar{\rho} \bar{u} \bar{v}) + j \frac{1}{y} (\bar{\rho} \bar{u} \bar{v}) = 0$$

and

$$\frac{\partial}{\partial t} (\bar{\rho} \bar{v}) + \frac{\partial}{\partial x} (\bar{\rho} \bar{u} \bar{v}) + \frac{\partial}{\partial y} (\bar{\rho} \bar{v}^2) + \frac{\partial \bar{p}}{\partial y} + j \frac{1}{y} (\bar{\rho} \bar{v}^2) = 0$$

Or

$$\frac{\partial}{\partial t} (\bar{\rho} \bar{u}) + \frac{\partial}{\partial x} (\bar{\rho} \bar{u}^2 + \bar{p}) + \frac{\partial}{\partial y} (\bar{\rho} \bar{u} \bar{v}) + j \frac{1}{y} (\bar{\rho} \bar{u} \bar{v}) = 0 \quad (15)$$

and

$$\frac{\partial}{\partial t} (\bar{\rho} \bar{v}) + \frac{\partial}{\partial x} (\bar{\rho} \bar{u} \bar{v}) + \frac{\partial}{\partial y} (\bar{\rho} \bar{v}^2 + \bar{p}) + j \frac{1}{y} (\bar{\rho} \bar{v}^2) = 0 \quad (16)$$

In the above Eqs. (14) to (16), $j=1$, if the axisymmetric flow system is treated. If otherwise, $j=0$.

Now, we consider the gas-particle interaction terms in gas-particle two-phase mixture flows. Here, the following space-averaged quantity,

$$\bar{f}_p = \frac{1}{\bar{S}_p} \sum \bar{N}_{pk} \quad (17)$$

is defined. The above summation is taken over the cloud whose centers $(\bar{x}_{pk}, \bar{y}_{pk})$ belong to the averaging domain \bar{S}_p . Thus, \bar{f}_p gives the number density \bar{n}_p at the center of the domain \bar{S}_p . The components of force exerted by the gas on all of the particles per unit volume are given by

$$\left. \begin{aligned} \bar{F}_{px} &= \bar{m}_p \frac{1}{\bar{S}_p} \sum \bar{N}_{pk} \bar{A}_{pk} (\bar{u} - \bar{u}_{pk}) \\ \bar{F}_{py} &= \bar{m}_p \frac{1}{\bar{S}_p} \sum \bar{N}_{pk} \bar{A}_{pk} (\bar{v} - \bar{v}_{pk}) \end{aligned} \right\} \quad (18)$$

Also, the total rate of heat \bar{Q}_p transferred from the gas to all of the particles per unit volume yields

$$\bar{Q}_p = \bar{m}_p \frac{1}{S_p} \sum \bar{N}_{pk} \bar{B}_{pk} (\bar{T} - \bar{T}_{pk}) \quad (19)$$

and the total rate of work \bar{W}_p done per unit volume of gas on all of the particles

$$\bar{W}_p = \bar{F}_{px} \bar{u} + \bar{F}_{py} \bar{v} - \bar{m}_p \frac{1}{S_p} \sum \bar{N}_{pk} \bar{A}_{pk} [(\bar{u} - \bar{u}_{pk})^2 + (\bar{v} - \bar{v}_{pk})^2] \quad (20)$$

Therefore, in the two-fluid model, the momentum equations for the gas-phase should be rewritten into

$$\frac{\partial}{\partial t}(\rho \bar{u}) + \frac{\partial}{\partial x}(\rho \bar{u}^2 + \bar{p}) + \frac{\partial}{\partial y}(\rho \bar{u} \bar{v}) + j \frac{1}{y}(\rho \bar{u} \bar{v}) + \bar{F}_{px} = 0 \quad (21)$$

and

$$\frac{\partial}{\partial t}(\rho \bar{v}) + \frac{\partial}{\partial x}(\rho \bar{u} \bar{v}) + \frac{\partial}{\partial y}(\rho \bar{v}^2 + \bar{p}) + j \frac{1}{y}(\rho \bar{v}^2) + \bar{F}_{py} = 0 \quad (22)$$

Furthermore, the energy equation for the gas-phase should also be described by taking into account the total rate of energy transferred per unit volume of gas to all of the particles. This becomes

$$\frac{\partial \bar{e}}{\partial t} + \frac{\partial}{\partial x} \{\bar{u}(\bar{e} + \bar{p})\} + \frac{\partial}{\partial y} \{\bar{v}(\bar{e} + \bar{p})\} + j \frac{\bar{v}}{y}(\bar{e} + \bar{p}) + \bar{Q}_p + \bar{W}_p = 0 \quad (23)$$

Rewriting the system of the above equations for a gas-phase interacting with a particle-phase in the vector form, it follows that

$$\frac{\partial \bar{Q}}{\partial t} + \frac{\partial \bar{F}}{\partial x} + \frac{\partial \bar{G}}{\partial y} + \bar{H} + \bar{H}_p = 0 \quad (24)$$

in which

$$\bar{Q} = \begin{bmatrix} \bar{\rho} \\ \bar{\rho} \bar{u} \\ \bar{\rho} \bar{v} \\ \bar{e} \end{bmatrix}, \quad \bar{F} = \begin{bmatrix} \bar{\rho} \bar{u} \\ \bar{\rho} \bar{u}^2 + \bar{p} \\ \bar{\rho} \bar{u} \bar{v} \\ \bar{u}(\bar{e} + \bar{p}) \end{bmatrix}, \quad \bar{G} = \begin{bmatrix} \bar{\rho} \bar{v} \\ \bar{\rho} \bar{u} \bar{v} \\ \bar{\rho} \bar{v}^2 + \bar{p} \\ \bar{v}(\bar{e} + \bar{p}) \end{bmatrix},$$

$$\vec{H} = \frac{1}{y} \begin{bmatrix} \bar{\rho} \bar{v} \\ \bar{\rho} \bar{u} \bar{v} \\ \bar{\rho} \bar{v}^2 \\ \bar{v}(\bar{e} + \bar{p}) \end{bmatrix}, \quad \vec{H}_p = \begin{bmatrix} 0 \\ \bar{F}_{px} \\ \bar{F}_{py} \\ \bar{Q}_p + \bar{W}_p \end{bmatrix} \quad (25)$$

In addition, the above system is supplemented by

$$\bar{p} = \bar{\rho} \bar{R} \bar{T} \quad (26)$$

$$\bar{c}^2 = \gamma \bar{R} \bar{T} \quad (27)$$

in which \bar{c} , \bar{R} and γ denote the speed of sound, gas constant ($\bar{R} = \bar{C}_{pg} - \bar{C}_{vg}$) and ratio of specific heats ($\gamma = \bar{C}_{pg} / \bar{C}_{vg}$), respectively.

2.3 Transformation to non-dimensional equations

Up to this point we have completed the system of equations governing the two-phase mixture flows on the dimensional space. Here, we wish to emphasize that in our calculation, the dimensionless variables and parameters are introduced, and the governing equations to be solved will be expressed by dimensionless quantities. It is physically important to rewrite the dimensional equations into dimensionless ones and to solve them in such a way as to realize the similarity of the flow pattern as well as the general validity. The main dimensionless variables introduced into the system of governing equations are defined as

$$\begin{aligned} t &= \frac{t}{\bar{L}/\bar{c}_r}, & x &= \frac{\bar{x}}{\bar{L}}, & y &= \frac{\bar{y}}{\bar{L}}, & \rho &= \frac{\bar{\rho}}{\bar{\rho}_r}, & p &= \frac{\bar{p}}{\bar{p}_r}, \\ u &= \frac{\bar{u}}{\bar{c}_r}, & v &= \frac{\bar{v}}{\bar{c}_r}, & T &= \frac{\bar{T}}{\bar{T}_r}, & c &= \frac{\bar{c}}{\bar{c}_r}, \\ x_p &= \frac{\bar{x}_p}{\bar{L}}, & y_p &= \frac{\bar{y}_p}{\bar{L}}, & u_p &= \frac{\bar{u}_p}{\bar{c}_r}, & v_p &= \frac{\bar{v}_p}{\bar{c}_r}, & T_p &= \frac{\bar{T}_p}{\bar{T}_r} \end{aligned} \quad (28)$$

where \bar{L} is the characteristic length of the flow system. One should keep in mind that the subscripts p and r , as mentioned already, denote particles and reference conditions, respectively. For example, \bar{c}_r is the speed of sound at a reference condition. Also, the velocity components of a particle located at (x_p, y_p) or (\bar{x}_p, \bar{y}_p) are denoted by u_p and v_p or \bar{u}_p and \bar{v}_p , respectively.

In addition to Eq. (28), for later convenience, we wish to define the following non-dimensional parameters;

$$\Gamma_r = \frac{\bar{\tau}_A}{\bar{\tau}_F}, \quad \Gamma_p = \frac{\bar{\rho}_{mp}}{\bar{\rho}_r}, \quad \nu_r = \frac{\bar{\rho}_p r}{\bar{\rho}_r} \quad (29)$$

$$\theta = \frac{\bar{C}_{pp}}{\bar{C}_{pg}} \quad (\bar{C}_{pp}: \text{Specific heat of particle material}) \quad (30)$$

Here, $\bar{\tau}_A$ is called the aerodynamic response time of a particle, assuming the Stokes drag law, and $\bar{\tau}_F$ the characteristic time of the flow system. These are defined by

$$\bar{\tau}_A = \frac{\bar{\rho}_{mp}(2\bar{r}_p)^2}{18\bar{\mu}}, \quad \bar{\tau}_F = \frac{\bar{L}}{\bar{c}_r} \quad (31)$$

in which the gas viscosity $\bar{\mu}$ is given by

$$\bar{\mu} = \bar{\mu}_r T^\delta \quad (\text{see Eq.(8)}) \quad (32)$$

where the exponent δ is taken to be 0.6.

We first consider the non-dimensionalization of Eqs. (9) and (10). Obviously, Eq. (9) becomes

$$\frac{d\bar{\mathbf{E}}_p}{dt} = \bar{\tau}_F \bar{\mathbf{I}}_p \quad (33)$$

Therefore, for Eq. (1) and Eq. (2), the following relations are easily obtained from Eq. (28)

$$\frac{dx_p}{dt} = u_p \quad (34)$$

$$\frac{dy_p}{dt} = v_p \quad (35)$$

Next, we make Eqs. (3) and (4) non-dimensional by taking Eq. (6) into consideration.

$$\begin{aligned} \frac{d}{dt}(\bar{c}u_p) &= \frac{9}{2} \frac{\bar{\mu}f_p}{\bar{\rho}_{mp}\bar{r}_p^2} \bar{c}_r(u-u_p) \bar{\tau}_F \\ &= \frac{f_p \bar{c}_r}{(\bar{\tau}_A/\bar{\tau}_F)} (u-u_p) \quad (\text{see Eq.(31)}) \end{aligned}$$

so that

$$\frac{du_p}{dt} = A_p(u-u_p) \quad (36)$$

$$\frac{dv_p}{dt} = A_p(v - v_p) \quad (37)$$

in which

$$A_p = f_p / \Gamma_\tau \quad (38)$$

Also, taking into consideration the relation that $\bar{h}_p = \bar{C}_{pp} \bar{T}_p$ and Eq. (6), rewriting Eq. (5), we have

$$\frac{d}{dt} (\bar{C}_{pp} \bar{T}_p) = \bar{\tau}_F \cdot \frac{3\bar{\mu} g_p \bar{C}_{pk}}{\bar{\rho}_{mp} \bar{r}_p^2 Pr} \bar{T}_p (T - T_p)$$

so that

$$\begin{aligned} \frac{dT_p}{dt} &= \left(\frac{9\bar{\mu}}{2\bar{\rho}_{mp} \bar{r}_p^2} \right) \cdot \frac{2}{3} \bar{\tau}_F \cdot \frac{g_p}{Pr\theta} (T - T_p) \\ &= \frac{2}{3} \frac{1}{(\bar{\tau}_A / \bar{\tau}_F)} \frac{g_p}{Pr\theta} (T - T_p) = B_p (T - T_p) \end{aligned} \quad (39)$$

in which

$$B_p = \frac{2g_p}{3\Gamma_\tau Pr\theta} \quad (40)$$

Accordingly, the system of non-dimensional equations for Eqs. (9) and (10) is given by

$$\frac{d\mathbf{E}_{pk}}{dt} = \mathbf{I}_{pk} \quad (41)$$

in which

$$\mathbf{E}_p = \begin{bmatrix} x_p \\ y_p \\ u_p \\ v_p \\ T_p \end{bmatrix} \quad \text{and} \quad \mathbf{I}_p = \begin{bmatrix} u_p \\ v_p \\ A_p(u - u_p) \\ A_p(v - v_p) \\ B_p(T - T_p) \end{bmatrix} \quad (42)$$

Next, we transform the system of equations for the gas-phase given in Eqs. (24) and (25) into the system of non-dimensional equations. First, we wish to define the following non-dimensional quantities for later convenience,

$$S_p = \frac{\bar{S}_p}{\bar{L}^2}, \quad N_p = \frac{\bar{N}_p}{\bar{n}_{pr} \bar{L}^2}, \quad \nu_r = \frac{\bar{n}_{pr} \bar{n}_p}{\bar{\rho}_r} \quad (43)$$

in which \bar{n}_p is the number density and $\bar{m}_p = (4/3) \pi \bar{r}_p^3 \bar{\rho}_{mp}$

First, the non-dimensionalization for \bar{e} , \bar{p} and \bar{c} (see Eqs. (12), (26) and (27)) is given by

$$e = \frac{\bar{p}}{\gamma(\gamma-1)} + \frac{1}{2}\rho(u^2 + v^2) \equiv \frac{\bar{e}}{\gamma\bar{p}_r} \quad (44)$$

$$\bar{p} = \rho T \quad (45)$$

$$c = T^{1/2} \quad (46)$$

Next, we rewrite \bar{F}_{px} and \bar{F}_{py} shown in Eq. (18), \bar{Q}_p in Eq. (19) and \bar{W}_p in Eq. (20) using Eqs. (6), (28), (40) and (43).

$$\begin{aligned} \bar{F}_{px} &= \frac{\nu_r \bar{\rho}_r}{S_p} \Sigma N_{pk} \frac{18\bar{\mu}}{\bar{\rho}_{mp}(2\bar{r}_p)^2} f_{pk} \bar{c}_r (u - u_{pk}) \\ &= \bar{c}_r \frac{\nu_r \bar{\rho}_r}{S_p} \Sigma N_{pk} \frac{1}{\bar{c}_A} f_{pk} (u - u_{pk}) \end{aligned} \quad (47)$$

$$\bar{F}_{py} = \bar{c}_r \frac{\nu_r \bar{\rho}_r}{S_p} \Sigma N_{pk} \frac{1}{\bar{c}_A} f_{pk} (v - v_{pk}) \quad (48)$$

and

$$\begin{aligned} \bar{Q}_p &= \frac{\nu_r \bar{\rho}_r}{S_p} \Sigma N_{pk} \frac{18\bar{\mu}}{\bar{\rho}_{mp}(2\bar{r}_p)^2} \cdot \frac{2}{3} \cdot \frac{g_{pk} \bar{C}_{pg}}{Pr} \bar{T}_r (T - T_{pk}) \\ &= \frac{\nu_r \bar{\rho}_r}{S_p} \Sigma N_{pk} \frac{2g_{pk}}{3(\bar{c}_A/\bar{c}_F)Pr\theta} \bar{C}_{pp} \frac{1}{\bar{c}_F} \bar{T}_r (T - T_{pk}) \\ &= \frac{\nu_r \bar{\rho}_r}{S_p} \Sigma N_{pk} B_{pk} \theta \frac{\gamma \bar{R}}{\gamma-1} \bar{T}_r (T - T_{pk}) \frac{1}{\bar{c}_F} \\ &= \frac{\bar{c}_r^2 \bar{\rho}_r}{\bar{c}_F} \frac{\nu_r}{S_p} \Sigma N_{pk} B_{pk} \frac{\theta}{\gamma-1} (T - T_{pk}) \end{aligned} \quad (49)$$

and

$$\begin{aligned} \bar{W}_p &= \bar{c}_r^2 \frac{\nu_r \bar{\rho}_r}{S_p} \{ u \Sigma N_{pk} \frac{f_{pk}}{\bar{c}_A} (u - u_{pk}) + v \Sigma N_{pk} \frac{f_{pk}}{\bar{c}_A} (v - v_{pk}) \} \\ &\quad - \bar{c}_r^2 \frac{\nu_r \bar{\rho}_r}{S_p} \Sigma N_{pk} \frac{f_{pk}}{\bar{c}_A} [(u - u_{pk})^2 + (v - v_{pk})^2] \\ &= \bar{c}_r^2 \bar{\rho}_r \frac{\nu_r}{S_p} [\{ u \Sigma N_{pk} \frac{f_{pk}}{\bar{c}_A} (u - u_{pk}) + v \Sigma N_{pk} \frac{f_{pk}}{\bar{c}_A} (v - v_{pk}) \} \\ &\quad - \Sigma N_{pk} \frac{f_{pk}}{\bar{c}_A} \{ (u - u_{pk})^2 + (v - v_{pk})^2 \}] \end{aligned} \quad (50)$$

According to Eq. (28), the non-dimensional continuity equation becomes

$$\frac{\bar{c}_r}{L} \frac{\partial}{\partial t} (\bar{\rho}_r \rho) + \frac{1}{L} \frac{\partial}{\partial x} (\bar{\rho}_r \rho \bar{c}_r u) + \frac{1}{L} \frac{\partial}{\partial y} (\bar{\rho}_r \rho \bar{c}_r v) + j \frac{1}{L y} (\bar{\rho}_r \rho \bar{c}_r v) = 0$$

so that

$$\frac{\partial \rho}{\partial t} + \frac{\partial}{\partial x} (\rho u) + \frac{\partial}{\partial y} (\rho v) + j \frac{\rho v}{y} = 0 \quad (51)$$

Combining Eq. (21) and Eq. (47) and introducing Eqs. (28) and (38), we have

$$\begin{aligned} \frac{\bar{c}_r}{L} \frac{\partial}{\partial t} (\bar{\rho}_r \rho \bar{c}_r u) + \frac{1}{L} \frac{\partial}{\partial x} (\bar{\rho}_r \rho \bar{c}_r^2 u^2 + \bar{p}_r \bar{p}) + \frac{1}{L} \frac{\partial}{\partial y} (\bar{\rho}_r \rho \bar{c}_r^2 uv) \\ + j \frac{1}{L} \frac{1}{y} (\bar{\rho}_r \rho \bar{c}_r^2 uv) + \bar{c}_r \frac{\nu_r \bar{\rho}_r}{S_p} \sum N_{pk} \frac{1}{\bar{\tau}_A} f_{pk} (u - u_{pk}) = 0 \end{aligned}$$

or

$$\begin{aligned} \bar{\rho}_r \bar{c}_r \frac{\partial}{\partial t} (\rho u) + \bar{\rho}_r \bar{c}_r \frac{\partial}{\partial x} (\rho u^2 + \frac{\bar{p}_r}{\bar{\rho}_r} \frac{\bar{p}}{\bar{c}_r^2}) + \bar{\rho}_r \bar{c}_r \frac{\partial}{\partial y} (\rho uv) \\ + j \bar{\rho}_r \bar{c}_r \frac{1}{y} (\rho uv) + \bar{c}_r \bar{\rho}_r \frac{\nu_r}{S_p} \sum N_{pk} \frac{f_{pk}}{\bar{\tau}_A / \bar{\tau}_F} (u - u_{pk}) = 0 \end{aligned}$$

so that

$$\begin{aligned} \frac{\partial}{\partial t} (\rho u) + \frac{\partial}{\partial x} (\rho u^2 + \bar{p} / \gamma) + \frac{\partial}{\partial y} (\rho uv) \\ + j \frac{1}{y} (\rho uv) + \frac{\nu_r}{S_p} \sum N_{pk} A_{pk} (u - u_{pk}) = 0 \end{aligned} \quad (52)$$

Similarly, we have

$$\begin{aligned} \frac{\partial}{\partial t} (\rho v) + \frac{\partial}{\partial x} (\rho uv) + \frac{\partial}{\partial y} (\rho v^2 + \bar{p} / \gamma) \\ + j \frac{1}{y} (\rho v^2) + \frac{\nu_r}{S_p} \sum N_{pk} A_{pk} (v - v_{pk}) = 0 \end{aligned} \quad (53)$$

Next, combining Eqs. (23), (44), (49) and (50), introducing Eqs. (28), (38) and (40), and noting that $\bar{c}_r^2 \bar{\rho}_r / \bar{\tau}_F = \gamma \bar{p}_r \bar{c}_r / L$, we have

$$\begin{aligned} \frac{\bar{c}_r}{L} \gamma \bar{p}_r \frac{\partial e}{\partial t} + \frac{1}{L} \frac{\partial}{\partial x} \{ \bar{c}_r u (\gamma \bar{p}_r e + \bar{p}_r \bar{p}) \} + \frac{1}{L} \frac{\partial}{\partial y} \{ \bar{c}_r v (\gamma \bar{p}_r e + \bar{p}_r \bar{p}) \} \\ + j \frac{\bar{c}_r}{L} \frac{v}{y} (\gamma \bar{p}_r e + \bar{p}_r \bar{p}) + \frac{\bar{c}_r^2}{\bar{\tau}_F} \cdot \frac{\nu_r \bar{\rho}_r}{S_p} \sum N_{pk} B_{pk} \frac{\theta}{\gamma - 1} (T - T_{pk}) \end{aligned}$$

$$\begin{aligned}
 & + \bar{c}_r^2 \frac{\nu_r \bar{\rho}_r}{S_p} \left[\{u \Sigma N_{pk} \frac{f_{pk}}{\bar{\tau}_A} (u - u_{pk}) + v \Sigma N_{pk} \frac{f_{pk}}{\bar{\tau}_A} (v - v_{pk})\} \right. \\
 & \left. - \Sigma N_{pk} \frac{f_{pk}}{\bar{\tau}_A} \{(u - u_{pk})^2 + (v - v_{pk})^2\} \right] = 0
 \end{aligned}$$

Rearranging the above equation yields

$$\begin{aligned}
 & \frac{\partial e}{\partial t} + \frac{\partial}{\partial x} \{u(e + p/\gamma)\} + \frac{\partial}{\partial y} \{v(e + p/\gamma)\} + j \frac{v}{y} (e + p/\gamma) \\
 & + \frac{\nu_r}{S_p} \Sigma N_{pk} B_{pk} \frac{\theta}{\gamma - 1} (T - T_{pk}) + \frac{\nu_r}{S_p} \left[\{u \Sigma N_{pk} A_{pk} (u - u_{pk}) \right. \\
 & \left. + v \Sigma N_{pk} A_{pk} (v - v_{pk})\} - \Sigma N_{pk} A_{pk} \{(u - u_{pk})^2 + (v - v_{pk})^2\} \right] \\
 & = 0
 \end{aligned} \tag{54}$$

Therefore, the system of non-dimensional equations for the gas-phase interacting with the particle-phase is given in the vector form by

$$\frac{\partial \mathbf{Q}}{\partial t} + \frac{\partial \mathbf{F}}{\partial x} + \frac{\partial \mathbf{G}}{\partial y} + \mathbf{H} + \mathbf{H}_p = 0 \tag{55}$$

in which

$$\begin{aligned}
 \mathbf{Q} &= \begin{bmatrix} \rho \\ \rho u \\ \rho v \\ e \end{bmatrix}, \quad \mathbf{F} = \begin{bmatrix} \rho u \\ \rho u^2 + p/\gamma \\ \rho uv \\ u(e + p/\gamma) \end{bmatrix}, \quad \mathbf{G} = \begin{bmatrix} \rho v \\ \rho uv \\ \rho v^2 + p/\gamma \\ v(e + p/\gamma) \end{bmatrix}, \\
 \mathbf{H} &= j \frac{1}{y} \begin{bmatrix} \rho v \\ \rho uv \\ \rho v^2 \\ v(e + p/\gamma) \end{bmatrix}, \quad \mathbf{H}_p = \begin{bmatrix} 0 \\ F_{px} \\ F_{py} \\ \dot{Q}_p + \dot{W}_p \end{bmatrix}
 \end{aligned} \tag{56}$$

Here, F_{px} , F_{py} , \dot{Q}_p and \dot{W}_p are defined by

$$F_{px} = \frac{\nu_r}{S_p} \Sigma N_{pk} A_{pk} (u - u_{pk}) \tag{57}$$

$$F_{py} = \frac{\nu_r}{S_p} \sum N_{pk} A_{pk} (v - v_{pk}) \quad (58)$$

$$\dot{Q}_p = \frac{\nu_r}{S_p} \sum N_{pk} B_{pk} \frac{\theta}{\gamma - 1} (T - T_{pk}) \quad (59)$$

$$\dot{W}_p = F_{px}u + F_{py}v - \frac{\nu_r}{S_p} \sum N_{pk} A_{pk} \{(u - u_{pk})^2 + (v - v_{pk})^2\} \quad (60)$$

Also, it should be borne in mind that $j=1$, if the flow system is axisymmetric, and that $j=0$ for the case where a two-dimensional Cartesian coordinate system is treated.

Finally, we note that C_D and Nu appearing in Eq. (7) are used on the basis of the Henderson correlating equation²¹⁾ and the empirical expression by Carlson and Høglund²²⁾, respectively.

3. Numerical scheme

3.1 Osher's scheme

The Euler equations of gas-phase, described in Eqs. (55) and (56), are solved using a second-order accurate TVD (Total Variation Diminishing) scheme developed by Chakravarthy and Osher^{6)~8)}. This is commonly called the Osher scheme. It is empirically well-known that the numerical quantities across a discontinuity exhibit a remarkable instability due to a false oscillatory property. A numerical overshooting or/and undershooting is commonly observed before and after the discontinuity. This scheme protect such numerical phenomena.

This section describes the outline of the Osher scheme according to Chakravarthy and Osher. It is worthwhile to take single phase (gas-only) flows for examples to aid the reader in understanding the applicability of this scheme, although the purpose of this paper is to investigate the two-phase flows.

In the scheme, the computational domain is divided into a number of small cells and the physical variables are defined at the cell center. Figure 1 indicates the cell arrangement in the x-direction and the flux difference between the cell interface and the centroidal grid point. One should bear in mind that for a two- or three-dimensional system, the one-dimensional Riemann problem with its simple solution is applied separately to each dimension. Thereby, independent discretizations of the flux derivatives in each spatial dimension are determined. Then, the terms are added up for the overall discretization. In this sense, we first consider only the flux in the x-direction. Thus, the first-order accurate flux at a cell interface $j+1/2$ (see Figure 1) is given by two kinds of forms as follows,

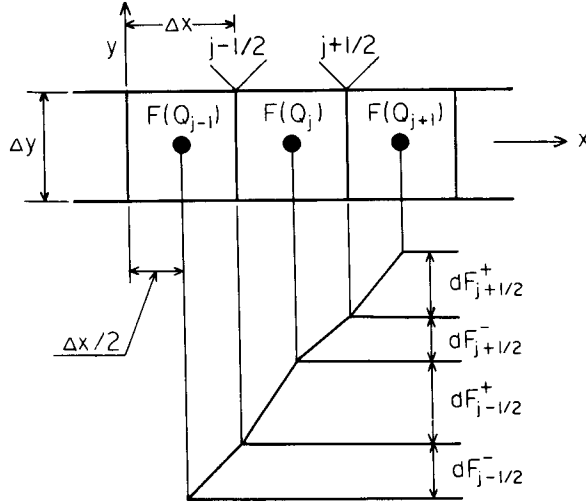


Fig. 1 Cell arrangement in the x-direction and flux difference between cell interface and centroidal grid point.

$$\tilde{F}_{j+1/2}^n = F^n(Q_j) + \sum_{i=1}^m dF_{j+1/2}^{in-} \quad (n=1\sim 4) \quad (61)$$

$$\tilde{F}_{j+1/2}^n = F^n(Q_{j+1}) - \sum_{i=1}^m dF_{j+1/2}^{in+} \quad (62)$$

so that

$$\tilde{F}_{j+1/2}^n = \frac{1}{2} (F_j^n + F_{j+1}^n - \sum_i dF_{j+1/2}^{in+} + \sum_i dF_{j+1/2}^{in-}) \quad (63)$$

in which Q_j (or Q_{j+1}) denotes the dependent variable which corresponds to the component of the vector, \mathbf{Q} , expressed in Eq. (56). Again, $F^n(Q_j)$ (or $F^n(Q_{j+1})$) is the flux determined by Q_j (or Q_{j+1}) ($F_j^n \equiv F^n(Q_j)$) and corresponds to the component of the vector, \mathbf{F} , in Eq. (56). m is the number of eigenvalues of the Jacobian matrix to be mentioned later. Also, the superscript + (or -) denotes the positive wave speed (or the negative one).

Next, we consider the spatial accuracy of the flux derivative when a semi-discrete approximation to $\partial\mathbf{Q}/\partial t + \partial\mathbf{F}/\partial x = 0$ is given by

$$\frac{\partial Q_j}{\partial t} + \frac{1}{\Delta x} (\tilde{F}_{j+1/2} - \tilde{F}_{j-1/2}) = 0 \quad (64)$$

In order to do so, we expand $dF_{j+1/2}^{i-}$ ($\equiv \sum_{i=1}^m dF_{j+1/2}^{i-}$) and $dF_{j-1/2}^{i+}$ ($\equiv \sum_{i=1}^m dF_{j-1/2}^{i+}$) in the Taylor series as

$$\begin{aligned}
dF_{j+1/2}^- &= \tilde{F}_{j+1/2} - F_j \quad (\text{see Eq.(61)}) \\
&= \frac{\Delta x}{2} \left(\frac{\partial F}{\partial x} \right)_j + \frac{(\Delta x)^2}{8} \left(\frac{\partial^2 F}{\partial x^2} \right)_j + O((\Delta x)^3)
\end{aligned} \tag{65}$$

$$\begin{aligned}
dF_{j-1/2}^+ &= F_j - \tilde{F}_{j-1/2} \quad (\text{see Eq. (62)}) \\
&= \left(\frac{\Delta x}{2} \right) \left(\frac{\partial F}{\partial x} \right)_j - \frac{(\Delta x)^2}{8} \left(\frac{\partial^2 F}{\partial x^2} \right)_j + O((\Delta x)^3)
\end{aligned} \tag{66}$$

so that

$$\begin{aligned}
\tilde{F}_{j+1/2} &= F_j + \left(\frac{\Delta x}{2} \right) \left(\frac{\partial F}{\partial x} \right)_j + \frac{(\Delta x)^2}{8} \left(\frac{\partial^2 F}{\partial x^2} \right)_j + O((\Delta x)^3) \\
\tilde{F}_{j-1/2} &= F_j - \left(\frac{\Delta x}{2} \right) \left(\frac{\partial F}{\partial x} \right)_j + \frac{(\Delta x)^2}{8} \left(\frac{\partial^2 F}{\partial x^2} \right)_j + O((\Delta x)^3)
\end{aligned} \tag{67}$$

Thereby

$$\frac{1}{\Delta x} (\tilde{F}_{j+1/2} - \tilde{F}_{j-1/2}) \simeq \left(\frac{\partial F}{\partial x} \right)_j + O((\Delta x)^2) \tag{68}$$

It is clear that the above approximation to the flux $\tilde{F}_{j\pm 1/2}$ is first-order accurate, while $(\partial F/\partial x)_j$ is second-order accurate. Again, the flux difference across the i -th wave, $dF_{j\pm 1/2}^\pm$ which appears in Eq. (63), can be obtained by solving a local Riemann problem with the left state s_j and the right state s_{j+1} .

According to the Riemann solver by Roe⁹⁾, dependent variables $s_{j+1/2}$ at each cell interface can be obtained using the two neighbouring cell states (s_j and s_{j+1}) as

$$s_{j+1/2} = \frac{s_{j+1}\sqrt{\rho_{j+1}} + s_j\sqrt{\rho_j}}{\sqrt{\rho_{j+1}} + \sqrt{\rho_j}} \tag{69}$$

Here, s represents ρ , u , v and $h (\equiv \bar{h}/\bar{c}_r^2 = p/((\gamma-1)\rho) + (u^2+v^2)/2 = c^2/(\gamma-1) + (u^2+v^2)/2)$ (see Eqs. (45) and (46)).

The approximate Riemann solver by Roe is based upon the linearized governing equation $\partial \mathbf{Q}/\partial t + A_{j+1/2} \partial \mathbf{Q}/\partial x = 0$, where A is the Jacobian matrix ($A_{j+1/2} = (\partial \mathbf{F}/\partial \mathbf{Q})_{j+1/2}$). Here, it should be borne in mind that the description of the scheme is limited to the two-dimensional Cartesian coordinate system, unless otherwise mentioned. Therefore, x - and y -axes to each cell interface are orthogonal with each other. Essentially, we have the two Jacobian matrices $A_1 = \partial \mathbf{F}/\partial \mathbf{Q}$ and $A_2 = \partial \mathbf{G}/\partial \mathbf{Q}$. But, using the generalized metrics n_x and n_y , which define the x - and y -components normal to the cell interface, the generalized Jacobian

matrix can be expressed by $A = n_x A_1 + n_y A_2$. Thus, $A = A_1 (n_x = 1 \text{ and } n_y = 0)$ in the x-direction because there is no contribution from the y-direction term. Of course, the same holds for the y-direction. In fact, the Jacobian matrix in the present situation can be expressed in the form of

$$A = \begin{pmatrix} 0 & n_x & n_y & 0 \\ \frac{n_x \Gamma}{2} q^2 - uU & U + n_x(1 - \Gamma)u & -V + n_x(1 - \Gamma)v & n_x \Gamma \\ \frac{n_y \Gamma}{2} q^2 - vU & V + n_y(1 - \Gamma)u & U + n_y(1 - \Gamma)v & n_y \Gamma \\ \Gamma U q^2 - \frac{\gamma e U}{\rho} & n_x \frac{\gamma e}{\rho} - \Gamma u U - \frac{n_x \Gamma}{2} q^2 & n_y \frac{\gamma e}{\rho} - \Gamma v U - \frac{n_y \Gamma}{2} q^2 & \gamma U \end{pmatrix} \quad (70)$$

in which

$$\left. \begin{aligned} q^2 &= u^2 + v^2 \\ U &= n_x u + n_y v \\ V &= n_x v - n_y u \\ \Gamma &= \gamma - 1 \end{aligned} \right\} \quad (71)$$

Also, the above matrix takes real eigenvalues in the form of the wave speed given by

$$\left. \begin{aligned} \lambda^1 &= U - c\sqrt{n_x^2 + n_y^2} \quad (c^2 = p/\rho) \\ \lambda^2 &= U \\ \lambda^3 &= U \\ \lambda^4 &= U + c\sqrt{n_x^2 + n_y^2} \end{aligned} \right\} \quad (72)$$

For these eigenvalues we have the two matrices L and R of the left and right eigenvectors as

$$L = \begin{pmatrix} l^1 \\ l^2 \\ l^3 \\ l^4 \end{pmatrix}$$

$$= \begin{pmatrix} \frac{\Gamma}{2c}q^2 + \hat{U} & -\hat{n}_x - \frac{\Gamma}{c}u & -\hat{n}_y - \frac{\Gamma}{c}v & \frac{\Gamma}{c} \\ -\frac{\Gamma}{2c}q^2 - \hat{V} + c & -\hat{n}_y + \frac{\Gamma}{c}u & \hat{n}_x + \frac{\Gamma}{c}v & -\frac{\Gamma}{c} \\ -\frac{\Gamma}{2c}q^2 + \hat{V} + c & \hat{n}_y + \frac{\Gamma}{c}u & -\hat{n}_x + \frac{\Gamma}{c}v & -\frac{\Gamma}{c} \\ \frac{\Gamma}{2c}q^2 - \hat{U} & \hat{n}_x - \frac{\Gamma}{c}u & \hat{n}_y - \frac{\Gamma}{c}v & \frac{\Gamma}{c} \end{pmatrix} \quad (73)$$

$$R = \begin{pmatrix} r^1 \\ r^2 \\ r^3 \\ r^4 \end{pmatrix}^T$$

$$= \frac{1}{2} \begin{pmatrix} \frac{1}{c} & \frac{1}{c} & \frac{1}{c} & \frac{1}{c} \\ \frac{u}{c} - \hat{n}_x & \frac{u}{c} - \hat{n}_y & \frac{u}{c} + \hat{n}_y & \frac{u}{c} + \hat{n}_x \\ \frac{v}{c} - \hat{n}_y & \frac{v}{c} + \hat{n}_x & \frac{v}{c} - \hat{n}_x & \frac{v}{c} + \hat{n}_y \\ \frac{q^2}{2c} - \hat{U} + \frac{c}{\Gamma} & \frac{q^2}{2c} + \hat{V} & \frac{q^2}{2c} - \hat{V} & \frac{q^2}{2c} + \hat{U} + \frac{c}{\Gamma} \end{pmatrix} \quad (74)$$

in which

$$\left. \begin{aligned} \hat{n}_x &= \frac{n_x}{\sqrt{n_x^2 + n_y^2}}, & \hat{n}_y &= \frac{n_y}{\sqrt{n_x^2 + n_y^2}} \\ \hat{U} &= \frac{n_x u + n_y v}{\sqrt{n_x^2 + n_y^2}} \\ \hat{V} &= \frac{n_x v - n_y u}{\sqrt{n_x^2 + n_y^2}} \end{aligned} \right\} \quad (75)$$

Now, we can easily derive on the basis of the orthogonality between L and R that

$$\begin{aligned} d\mathbf{F}_{j+1/2} &= A_{j+1/2}(\mathbf{Q}_{j+1} - \mathbf{Q}_j) \\ &= (R\Lambda R^{-1})_{j+1/2}(\mathbf{Q}_{j+1} - \mathbf{Q}_j) \\ &= (R\Lambda L)_{j+1/2}(\mathbf{Q}_{j+1} - \mathbf{Q}_j) \\ \Lambda &= \text{diag}(\lambda^i), \quad i=1 \sim 4 \end{aligned} \quad (76)$$

Here, $\text{diag}(\lambda^i)$ denotes a diagonal matrix with diagonal elements λ^i . Note that $A = R\Lambda L$. Thus, we have

$$\begin{pmatrix} dF_{j+1/2}^1 \\ dF_{j+1/2}^2 \\ dF_{j+1/2}^3 \\ dF_{j+1/2}^4 \end{pmatrix} = (R\Lambda)_{j+1/2} \begin{pmatrix} l_{j+1/2}^1 dQ \\ l_{j+1/2}^2 dQ \\ l_{j+1/2}^3 dQ \\ l_{j+1/2}^4 dQ \end{pmatrix} = R_{j+1/2} \begin{pmatrix} \lambda_{j+1/2}^1 \alpha_{j+1/2}^1 \\ \lambda_{j+1/2}^2 \alpha_{j+1/2}^2 \\ \lambda_{j+1/2}^3 \alpha_{j+1/2}^3 \\ \lambda_{j+1/2}^4 \alpha_{j+1/2}^4 \end{pmatrix} \quad (77)$$

in which

$$dQ = Q_{j+1} - Q_j = \begin{pmatrix} \rho_{j+1} - \rho_j \\ \rho_{j+1} u_{j+1} - \rho_j u_j \\ \rho_{j+1} v_{j+1} - \rho_j v_j \\ e_{j+1} - e_j \end{pmatrix} \quad (78)$$

$$\alpha_{j+1/2}^i = l_{j+1/2}^i dQ \quad (79)$$

Thus, Eq. (77) can be rewritten in the simple form of

$$\begin{pmatrix} dF^1 \\ dF^2 \\ dF^3 \\ dF^4 \end{pmatrix}_{j+1/2} = \begin{pmatrix} r^{11} \lambda^1 \alpha^1 + r^{12} \lambda^2 \alpha^2 + r^{13} \lambda^3 \alpha^3 + r^{14} \lambda^4 \alpha^4 \\ r^{21} \lambda^1 \alpha^1 + r^{22} \lambda^2 \alpha^2 + r^{23} \lambda^3 \alpha^3 + r^{24} \lambda^4 \alpha^4 \\ r^{31} \lambda^1 \alpha^1 + r^{32} \lambda^2 \alpha^2 + r^{33} \lambda^3 \alpha^3 + r^{34} \lambda^4 \alpha^4 \\ r^{41} \lambda^1 \alpha^1 + r^{42} \lambda^2 \alpha^2 + r^{43} \lambda^3 \alpha^3 + r^{44} \lambda^4 \alpha^4 \end{pmatrix}_{j+1/2} \\ = \begin{pmatrix} dF_{j+1/2}^{11} + dF_{j+1/2}^{12} + dF_{j+1/2}^{13} + dF_{j+1/2}^{14} \\ dF_{j+1/2}^{21} + dF_{j+1/2}^{22} + dF_{j+1/2}^{23} + dF_{j+1/2}^{24} \\ dF_{j+1/2}^{31} + dF_{j+1/2}^{32} + dF_{j+1/2}^{33} + dF_{j+1/2}^{34} \\ dF_{j+1/2}^{41} + dF_{j+1/2}^{42} + dF_{j+1/2}^{43} + dF_{j+1/2}^{44} \end{pmatrix} \quad (80)$$

in which r^{in} ($i = 1 \sim 4$; $n = 1 \sim 4$) corresponds to the element of the matrix given in Eq. (74) with the subscript $j + 1/2$, and $dF_{j+1/2}^{in} \equiv (\lambda^n \alpha^n r^{in})_{j+1/2}$, and

$$\left. \begin{aligned} \alpha_{j+1/2}^1 &= -\sqrt{\rho_j \rho_{j+1}} \Delta \hat{U}_{j+1/2} + \Delta p_{j+1/2} / \gamma / c_{j+1/2} \\ \alpha_{j+1/2}^2 &= \sqrt{\rho_j \rho_{j+1}} \Delta \hat{V}_{j+1/2} - \Delta p_{j+1/2} / \gamma / c_{j+1/2} + \Delta \rho_{j+1/2} c_{j+1/2} \\ \alpha_{j+1/2}^3 &= -\sqrt{\rho_j \rho_{j+1}} \Delta \hat{V}_{j+1/2} - \Delta p_{j+1/2} / \gamma / c_{j+1/2} + \Delta \rho_{j+1/2} c_{j+1/2} \\ \alpha_{j+1/2}^4 &= \sqrt{\rho_j \rho_{j+1}} \Delta \hat{U}_{j+1/2} + \Delta p_{j+1/2} / \gamma / c_{j+1/2} \end{aligned} \right\} \quad (81)$$

Here,

$$\left. \begin{aligned} \Delta \hat{U}_{j+1/2} &= \hat{U}_{j+1} - \hat{U}_j \\ \Delta \hat{V}_{j+1/2} &= \hat{V}_{j+1} - \hat{V}_j \\ \Delta p_{j+1/2} &= p_{j+1} - p_j \\ \Delta \rho_{j+1/2} &= \rho_{j+1} - \rho_j \end{aligned} \right\} \quad (82)$$

Now, we wish to note that $dF_{j+1/2}^{in}$ ($i = 1 \sim 4$; $n = 1 \sim 4$), which appears in Eq. (80), corresponds to the state changes across each simple wave. In short, the states at each cell interface can be calculated by Eq. (80). Furthermore, these flux differences may be redefined by introducing the concept of upwind differencing as

$$dF_{j+1/2}^{in+} = (\lambda^{i+} \alpha^i r^{in})_{j+1/2} = \left[\frac{1}{2} (\lambda^{i+} + |\lambda^i|) \alpha^i r^{in} \right]_{j+1/2} \quad (83)$$

and

$$dF_{j+1/2}^{in-} = (\lambda^{i-} \alpha^i r^{in})_{j+1/2} = \left[\frac{1}{2} (\lambda^{i-} - |\lambda^i|) \alpha^i r^{in} \right]_{j+1/2} \quad (84)$$

with the positive and negative parts of the eigenvalues. From Eqs. (83) and (84) we can determine the numerical flux function expressed in Eq. (63).

Again, the Roe scheme has the possibility to catch an expansion shock as well as the ordinary shocks, as Roe⁹⁾ and Chakravarthy¹⁰⁾ have pointed out. To avoid such a numerical situation, Matsuda et al.¹¹⁾ have followed the procedure developed by Chakravarthy, and proposed the following countermeasure for λ^{i+} and λ^{i-} : If at sonic expansion

$$\lambda_j^i < 0 \quad \text{and} \quad \lambda_{j+1}^i > 0 \quad (85)$$

then $\lambda_{j+1/2}^{i+}$ and $\lambda_{j+1/2}^{i-}$ in Eqs. (83) and (84) are required to be replaced by

$$\lambda_{j+1/2}^{i+} = \frac{1}{2} (\lambda_{j+1/2}^i + |\lambda_{j+1/2}^i|) + \frac{1}{4} (\lambda_{j+1}^i - \lambda_j^i) \quad (86)$$

$$\lambda_{j+1/2}^{i-} = \frac{1}{2} (\lambda_{j+1/2}^i - |\lambda_{j+1/2}^i|) - \frac{1}{4} (\lambda_{j+1}^i - \lambda_j^i) \quad (87)$$

The second-order Osher scheme treated here has no explicit artificial viscosity to suppress the unlimited flux difference across discontinuous waves such as shock wave, slip line, and contact surface. Thus, Chakravarthy and Osher have started with a one-parameter family of semi-discrete schemes with numerical flux,

$$\begin{aligned} \bar{F}_{j+1/2}^n = & \bar{F}_{j+1/2}^n - \frac{(1-\eta)}{4} (\sum_i dF_{j+3/2}^{in-}) - \frac{(1+\eta)}{4} (\sum_i dF_{j+1/2}^{in-}) \\ & + \frac{(1+\eta)}{4} (\sum_i dF_{j+1/2}^{in+}) + \frac{(1-\eta)}{4} (\sum_i dF_{j-1/2}^{in+}) \end{aligned} \quad (88)$$

and to obtain a higher-order TVD scheme, they have modified the last four

terms on the right hand side by utilizing flux limiters as

$$\begin{aligned} \hat{F}_{j+1/2}^n = & \tilde{F}_{j+1/2}^n - \frac{(1-\eta)}{4} (\sum_i \tilde{dF}_{j+3/2}^{in-}) - \frac{(1+\eta)}{4} (\sum_i \tilde{\tilde{dF}}_{j+1/2}^{in-}) \\ & + \frac{(1+\eta)}{4} (\sum_i \tilde{dF}_{j+1/2}^{in+}) + \frac{(1-\eta)}{4} (\sum_i \tilde{\tilde{dF}}_{j-1/2}^{in+}) \end{aligned} \quad (89)$$

with

$$\tilde{dF}_{j+3/2}^{in-} = \text{minmod}[dF_{j+3/2}^{in-}, \omega dF_{j+1/2}^{in-}] \quad (90a)$$

$$\tilde{dF}_{j+1/2}^{in-} = \text{minmod}[dF_{j+1/2}^{in-}, \omega dF_{j+3/2}^{in-}] \quad (90b)$$

$$\tilde{dF}_{j+1/2}^{in+} = \text{minmod}[dF_{j+1/2}^{in+}, \omega dF_{j-1/2}^{in+}] \quad (90c)$$

$$\tilde{\tilde{dF}}_{j-1/2}^{in+} = \text{minmod}[dF_{j-1/2}^{in+}, \omega dF_{j+1/2}^{in+}] \quad (90d)$$

and

$$1 \leq \omega \leq \frac{3-\eta}{1-\eta} \quad (91)$$

Also, it is noted that $\text{minmod}[a, b] = 0$, if $ab < 0$ and $\text{minmod}[a, b] = a$, if $|a| < |b|$. Otherwise, $\text{minmod}[a, b] = b$. Here, the spatial order of accuracy is determined by the value of η :

$\eta = -1$	fully upwind scheme
$\eta = 0$	Fromm Scheme
$\eta = 1/3$	third-order upwind-biased scheme

Eq. (89) is the Osher scheme to determine the numerical flux at $j+1/2$. Using the numerical solution for the Riemann problem obtained separately in each dimension, the dependent variables $Q_{j,k}^n(t+\Delta t)$ can be computed by

$$Q_{j,k}^n(t+\Delta t) = Q_{j,k}^n(t) - \frac{\Delta t}{\Delta x} (\hat{F}_{j+1/2}^n - \hat{F}_{j-1/2}^n) - \frac{\Delta t}{\Delta y} (\hat{F}_{k+1/2}^n - \hat{F}_{k-1/2}^n) \quad (92)$$

Thereby, all of the dependent variables $\mathbf{Q} = [\rho, \rho u, \rho v, e]^T$ can be evaluated at $t+\Delta t$ (Δt : time step). In the Osher scheme, the above Riemann problems are solved at every cell involved in a computational domain at every time step.

3.2 Numerical procedure

The numerical procedure of the Osher scheme described in the previous section is applied to a two-dimensional Cartesian coordinate system (or a one-dimensional system). We now consider the transformation of arbitrary coordinate systems. For convenience, we begin with

$$\frac{\partial \mathbf{Q}}{\partial t} + \frac{\partial \mathbf{F}}{\partial x} + \frac{\partial \mathbf{G}}{\partial y} = 0 \quad (\text{see Eq.(55)}) \quad (93)$$

and consider a transformation of variables of the type

$$\xi = \xi(x, y), \quad \eta = \eta(x, y) \quad (94)$$

So that

$$\left. \begin{aligned} \frac{\partial}{\partial x} &= \frac{\partial}{\partial \xi} \frac{\partial \xi}{\partial x} + \frac{\partial}{\partial \eta} \frac{\partial \eta}{\partial x}; & \partial_x &= \xi_x \partial_\xi + \eta_x \partial_\eta \\ \frac{\partial}{\partial y} &= \frac{\partial}{\partial \xi} \frac{\partial \xi}{\partial y} + \frac{\partial}{\partial \eta} \frac{\partial \eta}{\partial y}; & \partial_y &= \xi_y \partial_\xi + \eta_y \partial_\eta \end{aligned} \right\} \quad (95)$$

Thus, we have

$$\frac{1}{J} \frac{\partial \mathbf{Q}}{\partial t} + \frac{\xi_x}{J} \frac{\partial \mathbf{F}}{\partial \xi} + \frac{\eta_x}{J} \frac{\partial \mathbf{F}}{\partial \eta} + \frac{\xi_y}{J} \frac{\partial \mathbf{G}}{\partial \xi} + \frac{\eta_y}{J} \frac{\partial \mathbf{G}}{\partial \eta} = 0 \quad (96)$$

in which J is a Jacobian of transformation defined as

$$J = \frac{\partial(\xi, \eta)}{\partial(x, y)} = \xi_x \eta_y - \xi_y \eta_x \quad (97)$$

Again, obviously, the following relation holds true;

$$\begin{aligned} \partial_t \left(\frac{\mathbf{Q}}{J} \right) + \partial_\xi \left(\frac{\xi_x}{J} \mathbf{F} + \frac{\xi_y}{J} \mathbf{G} \right) + \partial_\eta \left(\frac{\eta_x}{J} \mathbf{F} + \frac{\eta_y}{J} \mathbf{G} \right) \\ = \mathbf{Q} \partial_t \left(\frac{1}{J} \right) + \mathbf{F} \partial_\xi \left(\frac{\xi_x}{J} \right) + \mathbf{G} \partial_\xi \left(\frac{\xi_y}{J} \right) + \mathbf{F} \partial_\eta \left(\frac{\eta_x}{J} \right) + \mathbf{G} \partial_\eta \left(\frac{\eta_y}{J} \right) \end{aligned} \quad (98)$$

By definition, it follows that

$$\begin{bmatrix} \partial_\xi \\ \partial_\eta \end{bmatrix} = J^{-1} \begin{bmatrix} \partial_x \\ \partial_y \end{bmatrix} \quad (\text{note } \partial_x \equiv \partial/\partial x, \text{ e. g.}) \quad (99)$$

Accordingly,

$$\begin{bmatrix} \partial_\xi \\ \partial_\eta \end{bmatrix} = \frac{1}{\xi_x \eta_y - \xi_y \eta_x} \begin{bmatrix} \eta_y & -\eta_x \\ -\xi_y & \xi_x \end{bmatrix} \begin{bmatrix} \partial_x \\ \partial_y \end{bmatrix} \quad (100a)$$

or

$$\left. \begin{aligned} \partial_\xi &= \frac{1}{J} (\eta_y \partial_x - \eta_x \partial_y) \\ \partial_\eta &= \frac{1}{J} (-\xi_y \partial_x + \xi_x \partial_y) \end{aligned} \right\} \quad (100b)$$

Self-evidently,

$$\left. \begin{aligned} x_{\xi} &= \frac{1}{J} \eta_y, & y_{\xi} &= -\frac{1}{J} \eta_x \\ x_{\eta} &= -\frac{1}{J} \xi_y, & y_{\eta} &= \frac{1}{J} \xi_x \end{aligned} \right\} \quad (101a)$$

or

$$\left. \begin{aligned} \xi_x &= J y_{\eta}, & \xi_y &= -J x_{\eta} \\ \eta_x &= -J y_{\xi}, & \eta_y &= J x_{\xi} \end{aligned} \right\} \quad (101b)$$

so that

$$J = \frac{1}{x_{\xi} y_{\eta} - x_{\eta} y_{\xi}} \quad (102)$$

Here, combining Eqs. (101 b) and (102) with the right hand side of Eq. (98) yields

$$\frac{\partial}{\partial t} \tilde{Q} + \frac{\partial}{\partial \xi} \tilde{F} + \frac{\partial}{\partial \eta} \tilde{G} = 0 \quad (103)$$

in which

$$\left. \begin{aligned} \tilde{Q} &= \frac{Q}{J} \\ \tilde{F} &= m_x F + m_y G \\ \tilde{G} &= n_x F + n_y G \\ m_x &= \frac{\xi_x}{J}, & m_y &= \frac{\xi_y}{J} \\ n_x &= \frac{\eta_x}{J}, & n_y &= \frac{\eta_y}{J} \end{aligned} \right\} \quad (104)$$

Furthermore, practically, for the cylindrical system of non-dimensional equations for the gas-phase interacting with the particle phase, which is given by Eq. (55), \mathbf{H} and \mathbf{H}_p should also be transformed in connection with Eq. (94). In this case, the system of equations is given, instead of Eq. (103), by

$$\frac{\partial \tilde{Q}}{\partial t} + \frac{\partial \tilde{F}}{\partial \xi} + \frac{\partial \tilde{G}}{\partial \eta} + \tilde{H} + \tilde{H}_p = 0 \quad (105)$$

and the following transformations,

$$\tilde{H} = \frac{H}{J}, \quad \tilde{H}_p = \frac{H_p}{J} \quad (106)$$

are supplemented besides Eq. (104).

Here, we should like to note that the axisymmetric term \tilde{H} and the gas-particle interaction term \tilde{H}_p are only additional terms in the equation of the two-dimensional gas-only flow and bear no direct relation to the TVD scheme.

In the present numerical procedure, the second-order accuracy in time is realized. We wish to describe briefly the prescription of the time-accuracy. Now, we introduce the discrete representation $x_i = x_0 + i\Delta x$ and $t_N = t_0 + N\Delta t$, and suppose that Q_i^N is some approximation to $Q(x_i, t_N)$. Then, we expand $Q(x_i, t_N + \Delta t/2)$ at the half time step into the following two kinds of Taylor series,

$$Q\left(x_i, t_N + \frac{\Delta t}{2}\right) = Q(x_i, t_N) + \frac{\Delta t}{2} \frac{\partial Q}{\partial t} + \frac{(\Delta t)^2}{8} \frac{\partial^2 Q}{\partial t^2} + O((\Delta t)^3)$$

$$Q\left(x_i, t_N + \frac{\Delta t}{2}\right) = Q(x_i, t_N + \Delta t) - \frac{\Delta t}{2} \frac{\partial Q}{\partial t} + \frac{(\Delta t)^2}{8} \frac{\partial^2 Q}{\partial t^2} + O((\Delta t)^3)$$

Thereby, the flow quantities $Q_i^{N+1/2}$ at the half time step $t_{N+1/2}$ can be evaluated by $(Q_i^N + Q_i^{N+1})/2$. Again, it is clear that the accuracy of $Q_i^{N+1/2}$ corresponds to the order of $(\Delta t)^2$. Thus, $Q_i^{N+3/2}$ can be easily obtained by using $Q_i^{N+1/2}$. Finally, Q_i^{N+1} is obtained in the form of

$$Q_i^{N+1} = \frac{1}{2}(Q_i^{N+1/2} + Q_i^{N+3/2}) \quad (107)$$

It should be stressed that throughout our numerical calculations to be mentioned later, the second-order accuracy in time is achieved by using Eq. (107).

Again, the time interval Δt is controlled by the Courant-Friedrichs-Lewy (CFL) condition. We simply consider the condition by the von Neumann stability analysis. We suppose a linear equation consisting of only the convection term such as $\partial Q/\partial t + U\partial Q/\partial x = 0$ in which the gas velocity U is a positive constant. Applying the forward difference to the unsteady term and the backward difference to the convection term

$$Q_i^{N+1} = Q_i^N - \beta \nabla Q_i^N = (E - \beta \nabla) Q_i^N \quad (108)$$

in which E and ∇ are the identity and backward operators, respectively, and $\beta (= U\Delta t/\Delta x)$ is commonly called the Courant number. According to von Neumann, he has put $Q_i^N = \exp(k_1 N\Delta t) \cdot \exp[k_2 j(i\Delta x)]$ ($j = \sqrt{-1}$) in the form of the Fourier series. Here, k_1 and k_2 are generally both the complex constants. Thus,

$$\begin{aligned}(E-\beta V)Q_i^N &= \exp(k_1 N \Delta t) [1 - \beta \{1 - \exp(-k_2 j \Delta x)\}] \exp[k_2 j (i \Delta x)] \\ &= \exp(k_1 \Delta t) \exp(k_1 N \Delta t) \exp[k_2 j (i \Delta x)]\end{aligned}$$

so that

$$\exp(k_1 \Delta t) = 1 - \beta \{1 - \exp(-k_2 j \Delta x)\} \equiv \lambda$$

As a result, the condition for the accumulative error not to increase as $N \rightarrow \infty$ is prescribed by $|\lambda| < 1$. That is, $0 < \beta \leq 1$. This means that Q can jump no more beyond one spatial mesh size ($\equiv \Delta x$) per time step Δt .

Practically, the integration time step Δt obeys

$$\Delta t = \beta \cdot \text{Min}\{\text{Min}(\Delta x, \Delta y) / (c + \sqrt{u^2 + v^2})\} \quad (109)$$

for every cell. In the present calculation, $\beta = 0.4$ is selected.

4. Numerical experiments

4.1 One-phase and two-phase jets exhausted from a sonic nozzle (I)

We begin with the one-phase jet flow problem. The Mach number of the jet at the nozzle exit is fixed to be $M_j = 1$. The jet begins to blow at $t = 0$ ($N = 0$) from an axisymmetric nozzle with 0.01 m in diameter at the exit. Again, we assume that a uniform ambient gas is at rest over the whole computational domain at $t = 0$.

In the present work, the characteristic length of the flow field \bar{L} is represented by the exit diameter of the nozzle ($\bar{D} = 1$ cm), and the reference conditions correspond to the reservoir conditions. The ratio of \bar{p}_0 to \bar{p}_∞ ($= \bar{p}_0 / \bar{p}_\infty$) is, in principle, fixed to be 5.8 ($\bar{p}_\infty = 1.0 \times 10^5$ Pa) and the temperature ratio $\bar{T}_0 / \bar{T}_\infty$ is fixed to be unity ($\bar{T}_\infty = 300$ K), where the subscripts, 0 and ∞ , denote the reservoir and ambient conditions. Again, the gas flow from the reservoir to the nozzle exit is assumed to be isentropic. Hence, the gas pressure, \bar{p}_j , at the nozzle exit is obtained through an isentropic relationship from the stagnation conditions;

$$\bar{p}_j = \bar{p}_0 \left[1 + \frac{\gamma - 1}{2} M_j^2 \right]^{-\gamma / (\gamma - 1)} \quad (110)$$

Also, in the two-phase jet flows to be mentioned later, the so-called mist composed of air and water-particles will be treated as the representation of gas-particle two-phase mixtures. The physical constants of the gas and the particles adopted are listed in Table 1. For the present case of one-phase jet flows,

Table.1 Physical constants of gas and particles.

Gas (Air)	$\bar{\rho}_{mp} = 1000 \text{ kg/m}^3$
$\gamma = 1.4$	$\bar{C}_{pp} = 4187 \text{ J/(kg}\cdot\text{K)}$
$\bar{C}_w = 1004 \text{ J/(kg}\cdot\text{k)}$	$\bar{r}_p = 10 \text{ }\mu\text{m}$
$\bar{T}_0 = 300 \text{ K}$	
$Pr = 0.7$	
$\bar{\mu} = 2.07 \times 10^{-5} \text{ Pa}\cdot\text{s}$ (at \bar{T}_0)	

the gas condition is assumed to be the same as shown in Table 1. Therefore, the condition that $M_j = 1$ gives the pressure ratio $\bar{p}_j/\bar{p}_0 = 0.528$. That is, $\bar{p}_j/\bar{p}_\infty = 3.062$.

The computational domain is divided into 150×100 meshes (or cells) in the x- and y-directions, respectively. The nozzle axis is taken along the x-axis and the radial direction along the y-axis (see Figure 2). Again, the mesh size, Δx ($=\Delta y$) is selected at 0.05.

Here, we wish briefly to mention the boundary condition of the computational domain in the present calculation. As Matsuda et al.¹²⁾ have pointed out, because the Osher scheme has no explicit artificial viscosity to cut down unphysical disturbances, the numerical results are rather sensitive to the choice of the boundary condition imposed on the numerical boundaries, which may produce or reflect unrealistic damage to the main flow. According to their results obtained by several boundary conditions, it follows that the imposition of the ambient gas condition to the upstream boundary BC, the downstream one DE and the side one CD gives a best-fit to the realistic phenomena encountered in the experimental results (see Figure 2).

As has been mentioned already, the physical variables are defined at the cell center in the cell method. So that, we must take two additional cells just outside the interior cells contacting the boundaries so that the fluxes just on the boundaries may be calculated by solving a Riemann problem between the state in the additional cell and the state in the cell just inside the boundary. In short, the Riemann problems must be solved at every cell and at every time step strictly (see Eq. (89)).

In the above ambient gas condition, the additional cells are filled with an ambient gas.

The symmetric condition is applicable to the jet axis, AE (see Figure 2). This is the condition that only the velocity component (v in the present situa-

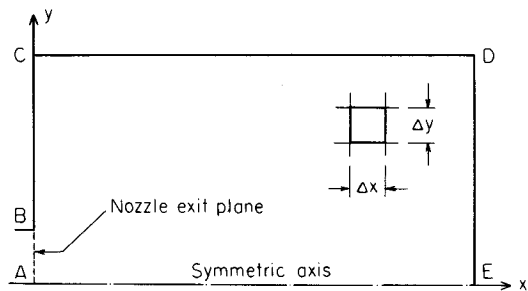


Fig. 2 Computational domain. Note that it is divided into 150×100 meshes in the x - and y -direction, respectively ($\Delta x = \Delta y = 0.05$).

tion) normal to the jet axis is opposite through the boundary AE, and the other physical quantities such as ρ , u , e are taken to be equal between the interior and exterior cells next to the axis AE. This symmetric condition is applicable to a solid wall surface, also when the gas flow around an object is treated.

The jet condition is applied to the jet exit plane AB. This is the condition that ρ , u , v and e of the jet at the nozzle exit are input to the exterior cells contacting with the jet exit boundary.

Now, we wish to present calculated results of the one-phase free jet. Figure 3 indicates the density contours ($N = 5000$) for underexpanded choked free jets of the four cases where $p_0 = 5.8 \times 10^5$ Pa(a), $p_0 = 10.0 \times 10^5$ Pa(b), $p_0 = 15.0 \times 10^5$ Pa(c) and $p_0 = 19.4 \times 10^5$ Pa(d). These calculations were continued till $N = 10000$ in order to check whether the global shock cell structures can reach a steady or converged stage with time (as $N \rightarrow \infty$). We have confirmed that the flow field upstream from the Mach disk is stable and steady, and the characteristics of the first shock cell remain unvaried with time. However, the flow field downstream from the Mach disk is not time-independent but considerably unsteady. This situation is reproduced by the time history of the density distribution along the symmetric axis. Figure 4 shows the numerical results obtained for $8020 \leq N \leq 10000$ under the corresponding conditions mentioned above. Here, the time history is taken at every 20 time steps. This demonstrates that an almost steady flow field is constricted only to the region upstream from the Mach disk for the large N , while in the region downstream from the Mach disk, the density field is appreciably fluctuating or oscillatory, even for the large N . This situation is not always unlikely. At a high Reynolds number, the jet boundary is very unstable and therefore the jet usually experiences a self-sustained oscillation due to a

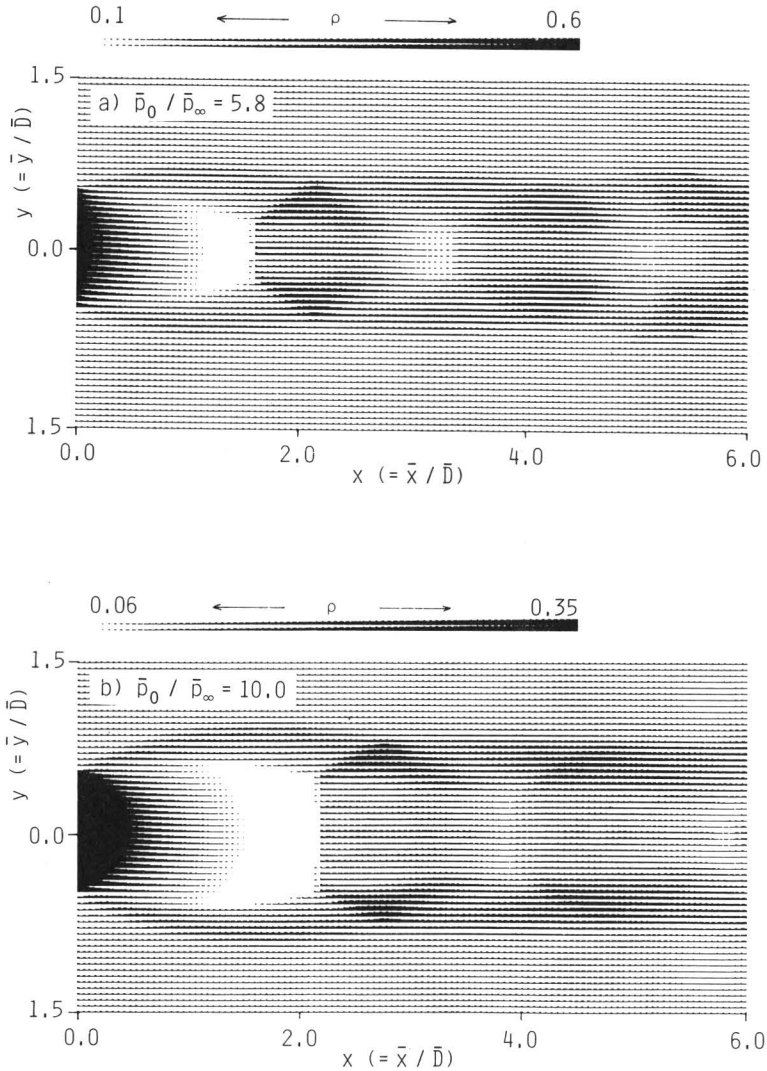


Fig. 3 For caption see next page.

feedback mechanism in connection with the radiation of the screech tone^{13), 14)}.

One of the most important factors here is to examine whether or not the present numerical scheme is applicable to and valid for the calculation of the flow field of the relatively simple one-phase free jets. If no check is made for the scheme, the numerical results of the more complicated flow field do not always enable us to be convinced. Thus, a few points of characteristics of the

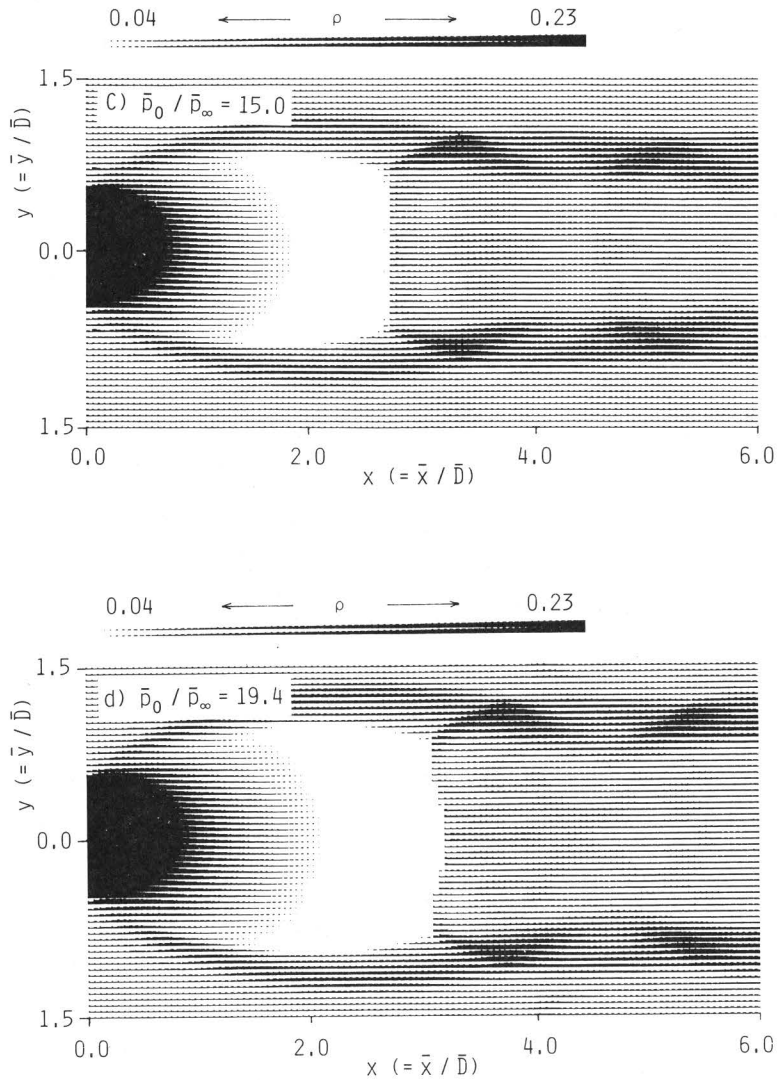


Fig. 3 Contours of constant density for underexpanded choked sonic jets of the four cases where $\bar{p}_0 = 5.8 \times 10^5$ Pa (a), $\bar{p}_0 = 10.0 \times 10^5$ Pa (b), $\bar{p}_0 = 15 \times 10^5$ Pa (c) and $\bar{p}_0 = 19.4 \times 10^5$ Pa (d).

first shock cell structure calculated are compared with the experiments of Love et al.¹⁵⁾. That is, the ratio of the distance \bar{L}_m from the nozzle exit to the Mach disk to the diameter \bar{D} of the nozzle exit, the ratio of the diameter of the Mach disk \bar{D}_m to \bar{D} , and the ratio of the wave length \bar{L}_w to \bar{D} are shown against \bar{p}_j/\bar{p}_∞ in Figure 5 (a), and therein compared with the experimental results. The comparison gives excellent agreement between the calculated and the experimen-

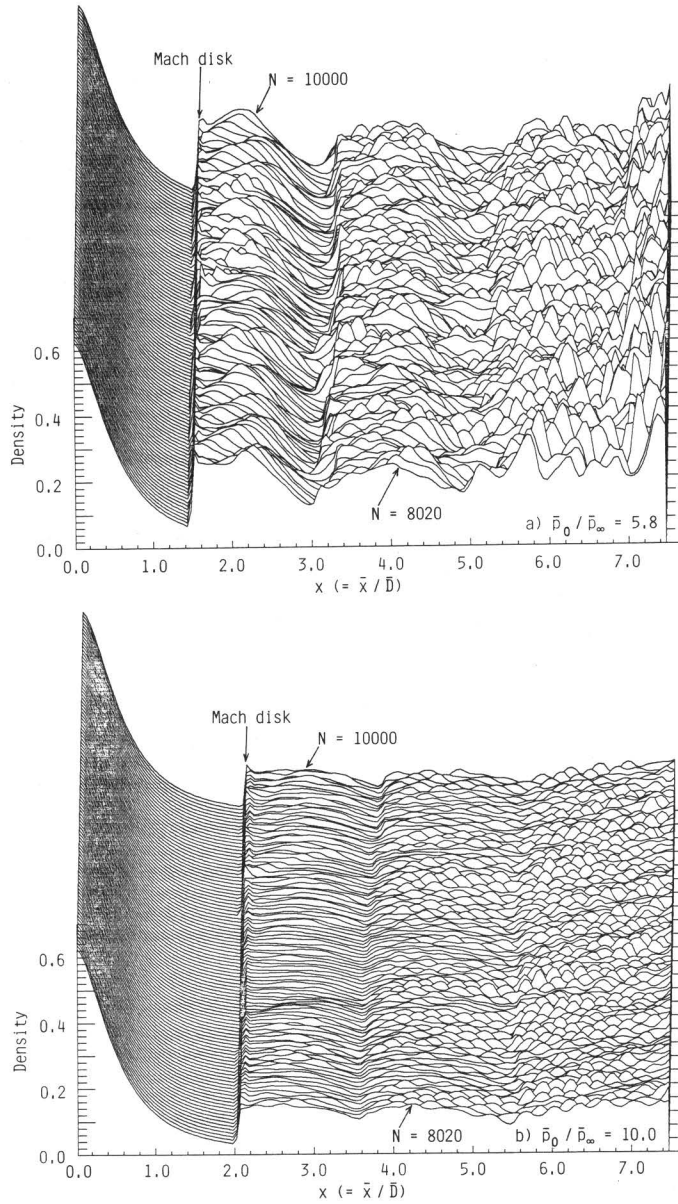


Fig. 4 For caption see next page.

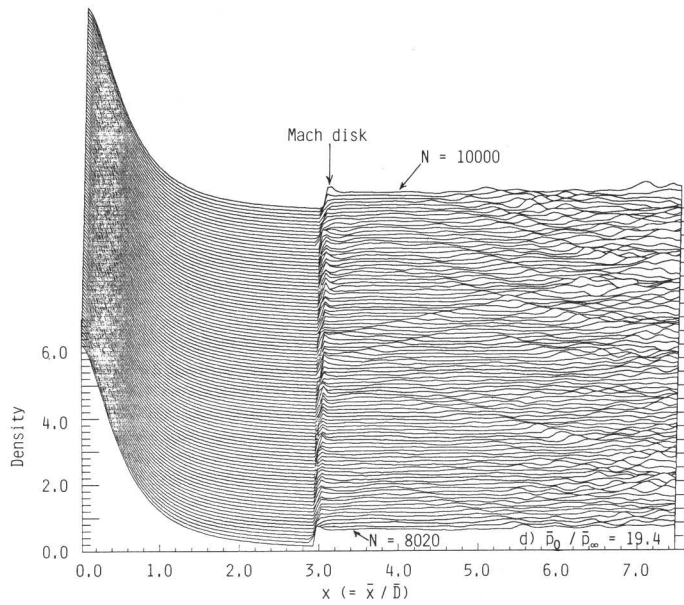
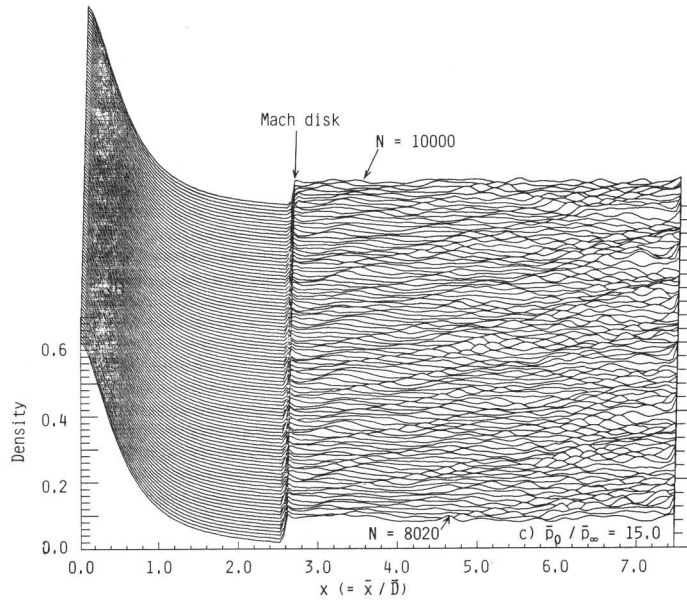


Fig. 4 Time history of density distribution along jet axis for $8020 \leq N \leq 10000$ under the conditions corresponding to Fig. 3.

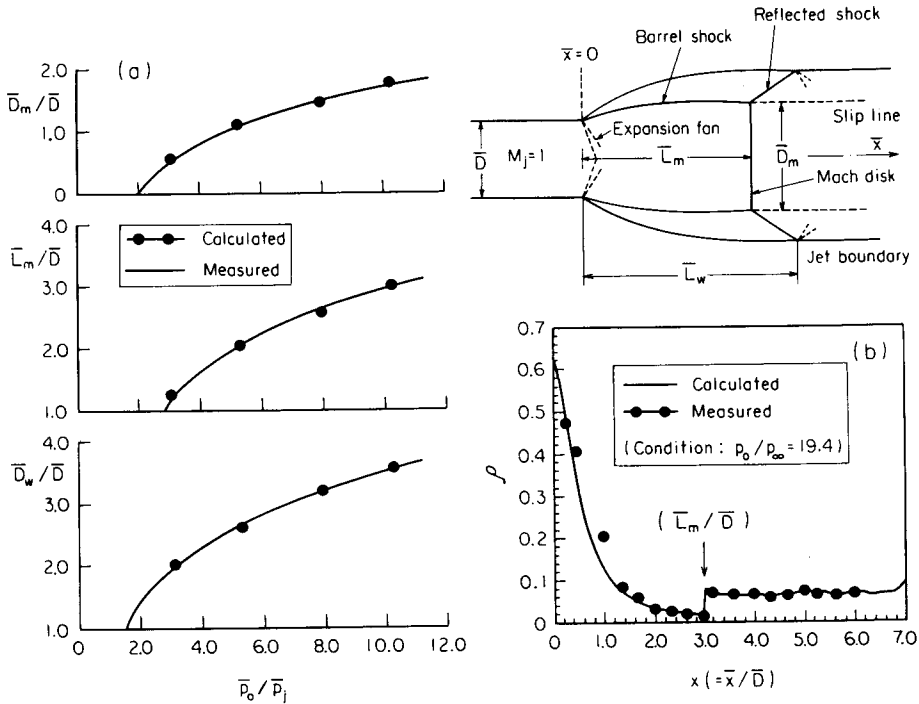


Fig. 5 Comparison of the present dust-free results with experiments for characteristics of the first shock cell (a) and density distribution along the jet axis (b).

tal results. Next, the density distribution along the jet axis, which has been computed under the condition that the pressure ratio $\bar{p}_0/\bar{p}_\infty = 19.4$, is compared with the experimental results measured under the same condition by Kobayashi et al.¹⁶⁾. The comparison is shown in Figure 5 (b) and gives fairly good agreement between the two results. These two facts suggest that the present numerical scheme may well simulate various complicated flow fields, at least, the flow structure of a free jet.

Now, we consider two-phase jet flows exhausted from a sonic jet. It is assumed here that in a nozzle the particle phase is in velocity and thermal equilibrium with the gas-phase. So, both the velocity and the temperature of particles at the nozzle exit are assumed to be equal to those of the gas. On this premise the particles are injected into the one-phase jet at fixed points on the nozzle exit plane at each time step after the final time step ($N = 10000$) in the one-phase solution. The case is selected where the pressure ratio is taken to be $\bar{p}_0/\bar{p}_\infty = 5.8$. Therefore, when the particles are initially injected into a gas jet flow, the state of the density field of the gas is the same as in Figure 3 (a).

Concerning the positions where the particles are injected, we divide the nozzle radius equally into K parts and put the particle subclouds at the center of each part. So, in the present numerical experiment, it follows that K particle subclouds are injected into the flow field at each time step. Here, we consider the number of particles contained in a subcloud. The time interval Δt determined by the CFL condition for the gas-phase flow is also applicable to the particle-phase analysis. Let us denote the axial and radial sizes of the k -th particle subcloud by Δx_p^\dagger and Δy_p^\dagger , respectively. These can be rewritten into

$$\begin{aligned}\Delta x_p^\dagger &= |\bar{u}_p| \cdot |\Delta t| = \bar{c}_r |\mathbf{u}_p| \cdot \frac{\bar{L}}{\bar{c}_r} \Delta t = |\mathbf{u}_p| \Delta t \bar{L} \\ \Delta y_p^\dagger &= y_p/K = \bar{L}(y_p/\bar{L})/K = \Delta y_p \bar{L}\end{aligned}\tag{111}$$

by the definition of Eq. (28). Thus, the number of particles per unit length of a ring subcloud can be counted by

$$\bar{N}_p^\dagger = \bar{n}_p^\dagger \Delta x_p \Delta y_p = \bar{n}_p^\dagger |\mathbf{u}_p| \Delta t \Delta y_p \bar{L}^2\tag{112}$$

Thus, as defined in Eq. (43)

$$N_p^\dagger = |\mathbf{u}_p| \Delta t \cdot \Delta y_p^\dagger\tag{113}$$

or

$$N_p = (y_p^\dagger/y_p) N_p^\dagger \quad (\text{see Eq. (11)})\tag{114}$$

The number of subclouds K injected into a flow field at each time step is always kept unvariable. In the present case, $K=25$ is taken, and therefore $\Delta y_p = \Delta y/2.5$. Therefore, although the condition that $\Delta y_p \ll \Delta y$ is not necessarily satisfied, it is automatically satisfied that $|\mathbf{u}_p| \Delta t$ is much smaller than the mesh size Δx . It may be considered that $\Delta S_p = \Delta x_p \cdot \Delta y_p$ is sufficiently small in comparison with the space-averaged area $S_p = \Delta x \cdot \Delta y$.

Now, we wish to show some characteristics of the jet flow of the gas-particle mixture for the loading ratio $\nu=0.3$ and the particle radius $\bar{r}_p = 10 \mu\text{m}$. Figure 6 shows the comparison of the density contour of the two-phase mixture flows with the corresponding dust-free ones at several kinds of time steps. At the first glance, a significant discrepancy can not be observed between the two flows. It need not take so large a number of time steps to get a roughly time-converged solution after the injection of the particle subcloud into the flow field. One should bear in mind that the first step ($N=1$) actually corresponds to $N=10001$, because the dust-free result obtained at $N=10000$ is employed as the

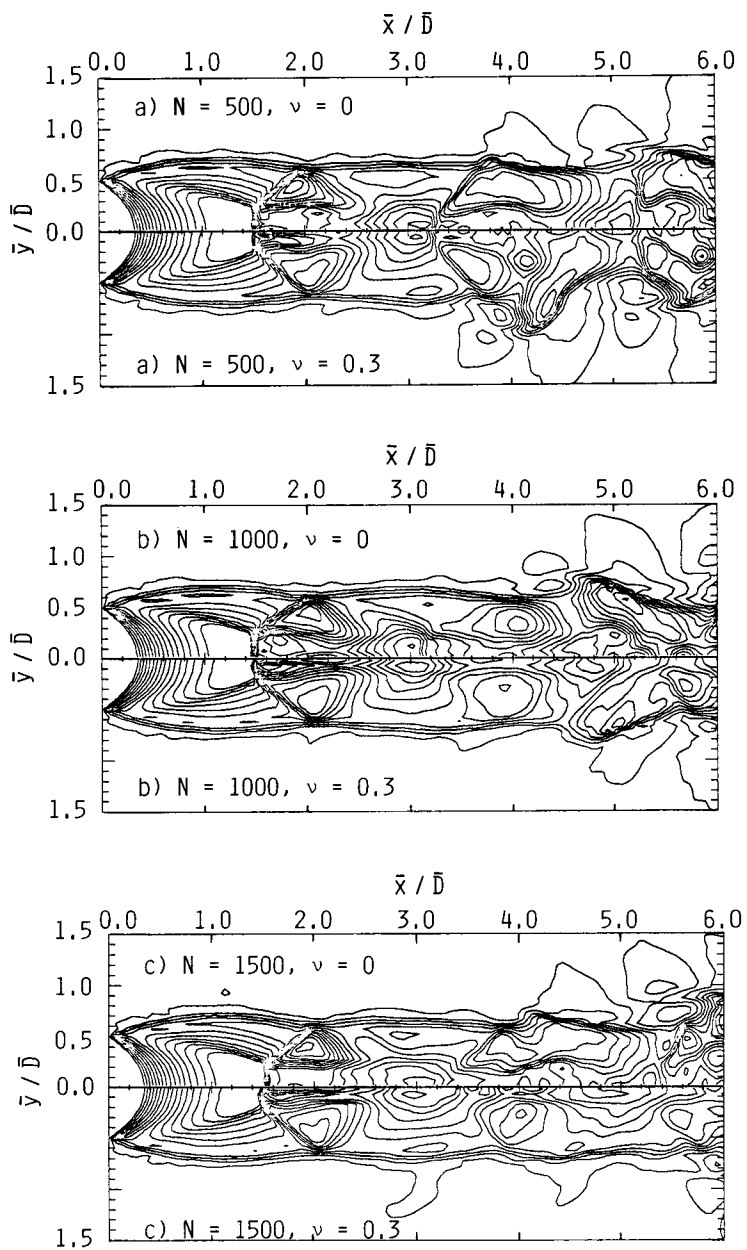


Fig. 6 For caption see next page.

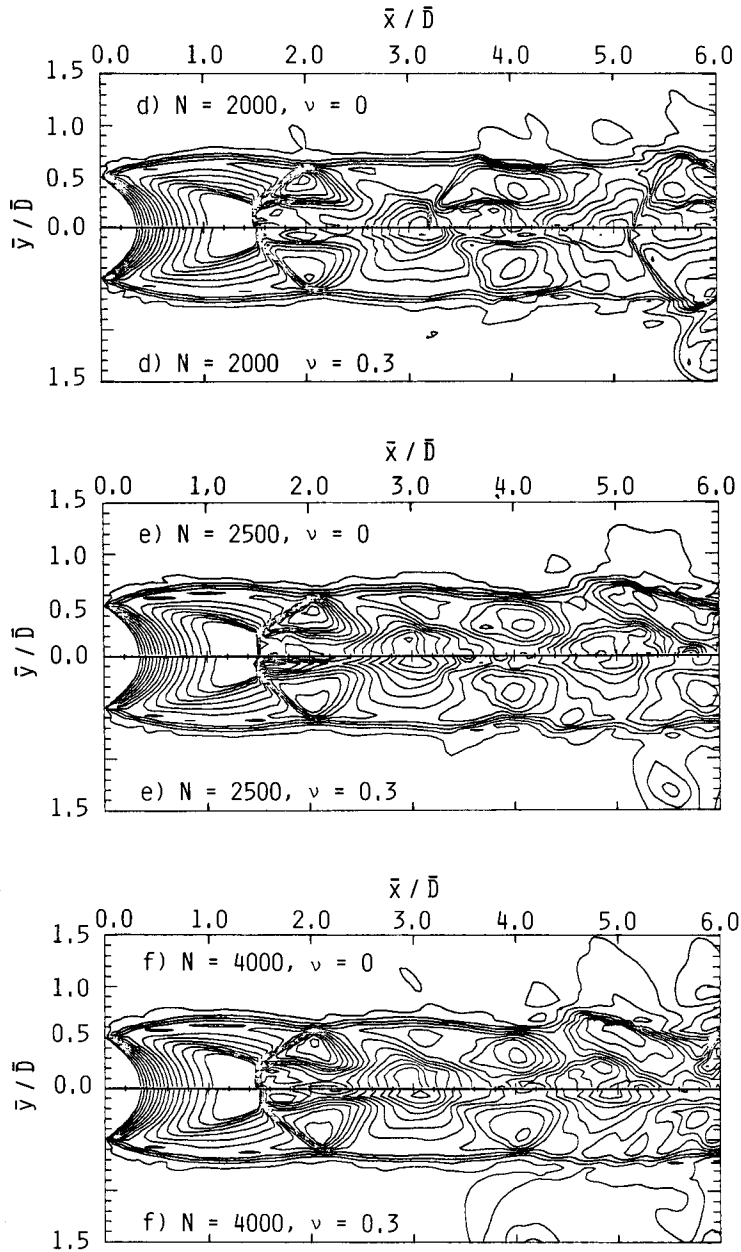


Fig. 6 Comparison of density contour of two-phase mixture flows with the corresponding dust-free ones at several kinds of time steps.

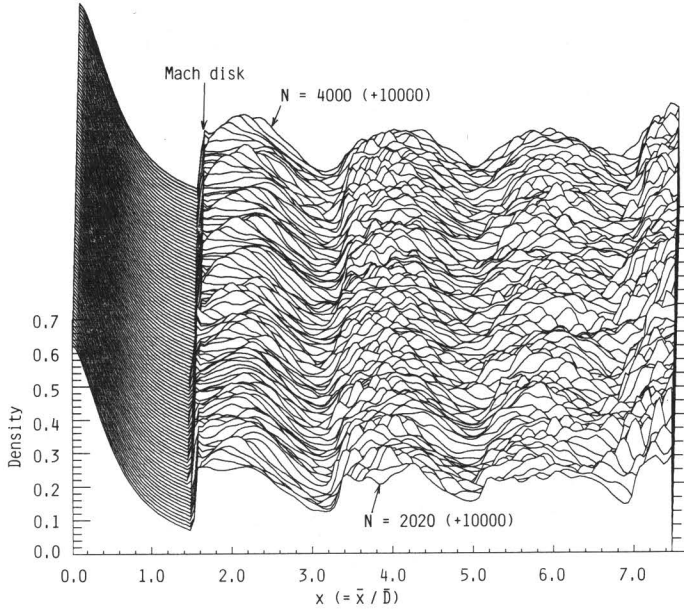


Fig. 7 Time history of density distribution of two-phase flow along the jet axis for $2020 \leq N \leq 4000$.

initial flow condition. First, the location of the Mach disk of the two-phase results tends to move more remarkably than that of the one-phase results, although it is slight. Also, the jet boundary downstream from the Mach disk is somewhat unstable for both the one-phase and two-phase flows.

Figure 7 shows the time history of the density distribution of two-phase flow along the symmetric axis for $2020 \leq N \leq 4000$ at every 20 time steps. According to this figure, the fluctuating motion of density in the jet core downstream from the Mach disk seems to be suppressed in comparison with the one-phase result (see Figure 4 (a)), although it is not so remarkable. Figure 8 demonstrates the variation of the velocity vectors of particles along streaklines in the two-phase jet flows with time, at the time steps corresponding to the case of Figure 6. Although a partly unstable aspect can be observed, neither coalescence nor intersection takes place in the whole flow field. Presumably, this may be based on the fact that the particle size is taken to be a little too large ($\bar{r}_p = 10 \mu\text{m}$). Again, the flow field of particles is enlarged in the radial direction as the particles proceed downstream.

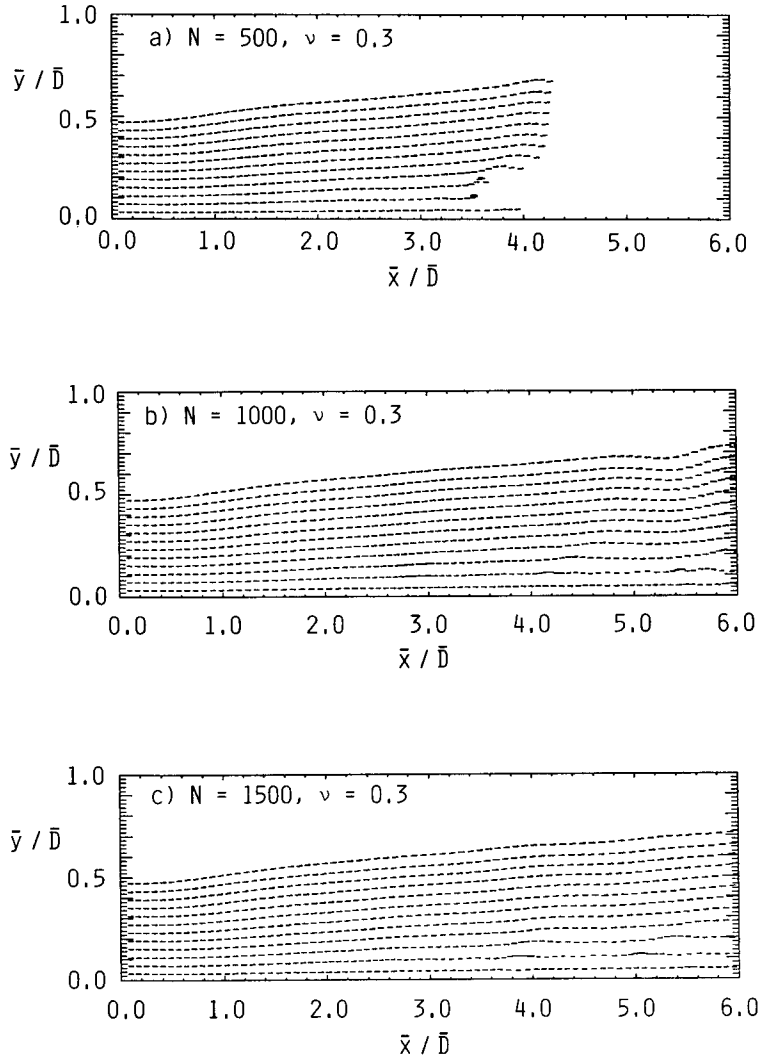


Fig. 8 For caption see next page.

4.2 One-phase and two-phase jets impinging on a disk (II)

This section describes some characteristics in the flow field of the one-phase and two-phase jets impinging on a disk perpendicular to the jet axis. The computational conditions are almost the same as those of section 4.1, except that a disk stands in the flow field. The diameter and thickness of the disk are taken to be equal to the diameter and thickness of the disk are taken to be equal to

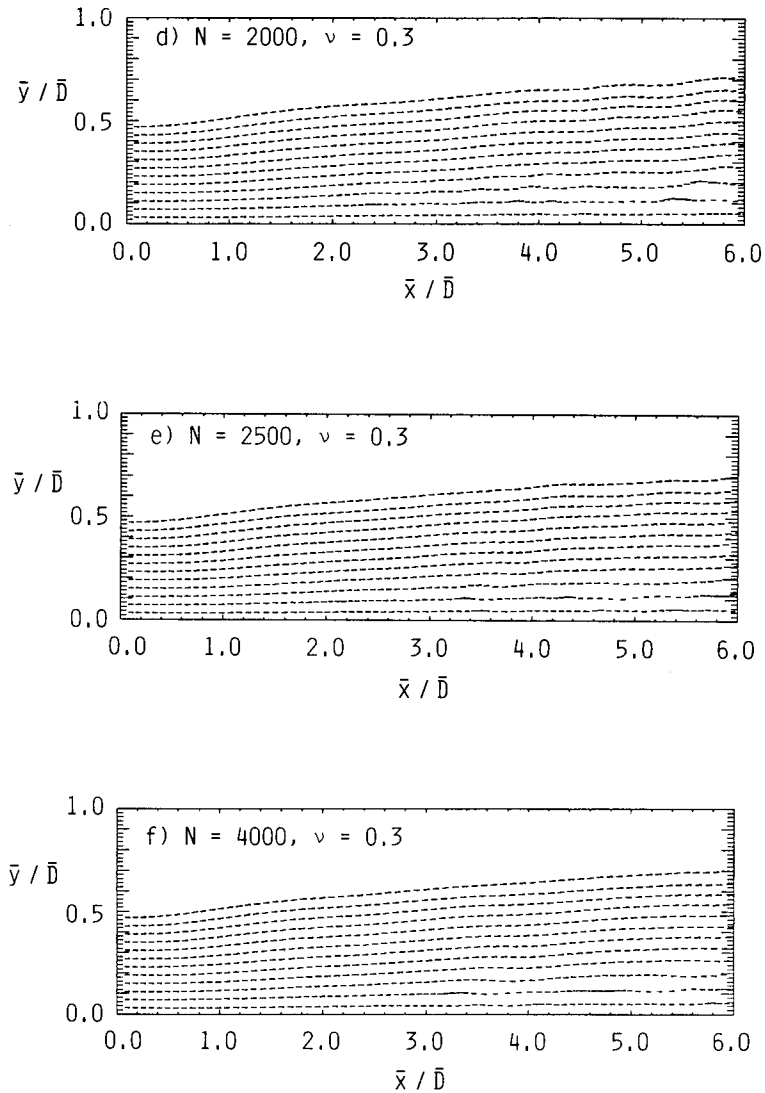


Fig. 8 Fields of velocity vectors of particles along streaklines at the time steps corresponding to the case of Fig. 6.

the diameter of the nozzle exit ($\bar{D} = 10$ cm) and $\bar{D}/2$, respectively. It is assumed that the disk stands at the distance of $x(=\bar{x}/\bar{D}) = 3$ from the nozzle exit.

We begin with the comparison of the flow fields between the one-phase and two-phase cases. Figure 9 shows the comparison of the density contours between the two cases at a few kinds of time steps. The flow field in the region upstream from the Mach disk is seen to be relatively stable. However, in the

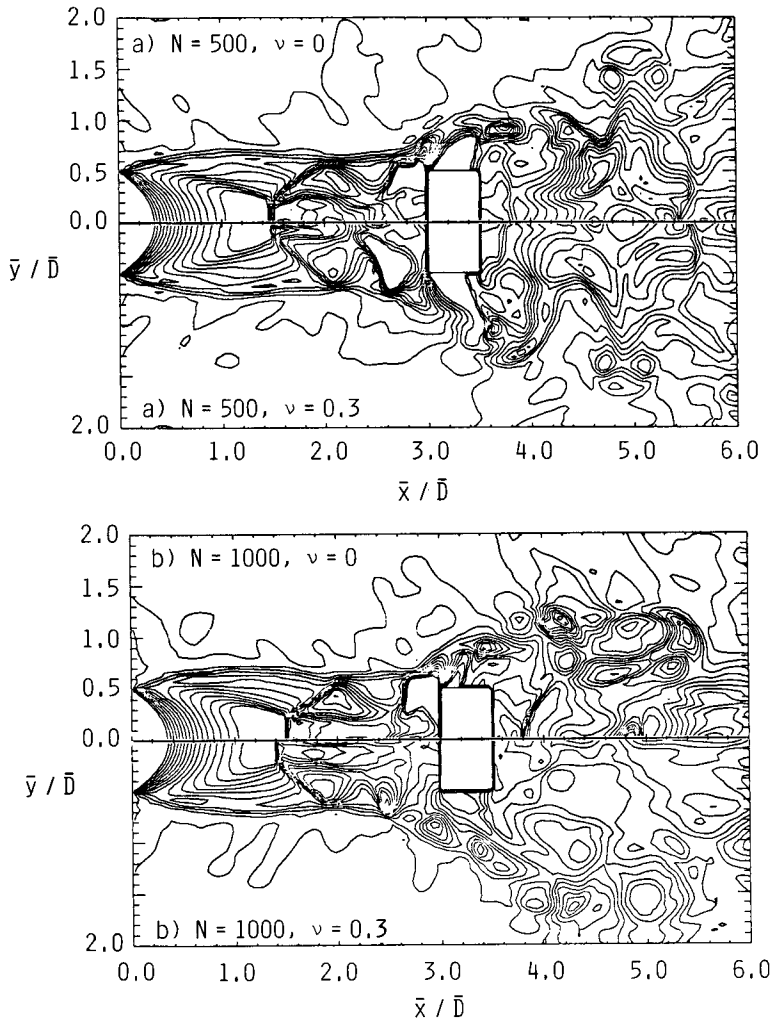


Fig. 9 For caption see next page.

region downstream from the Mach disk, in particular behind the disk, many small and large vortical structures are observed, and the jets interacting with the disk fluctuate in a very unstable state in comparison with the previous case where the disk is not present. Again, the jet boundaries, which can not clearly be discriminated, are enlarged in the radial direction after the impingement of the jet core on the disk. Such a tendency is understood to be more notable in the two-phase result than in the one-phase one.

Figure 10 indicates the comparison of the time history of the density dis-

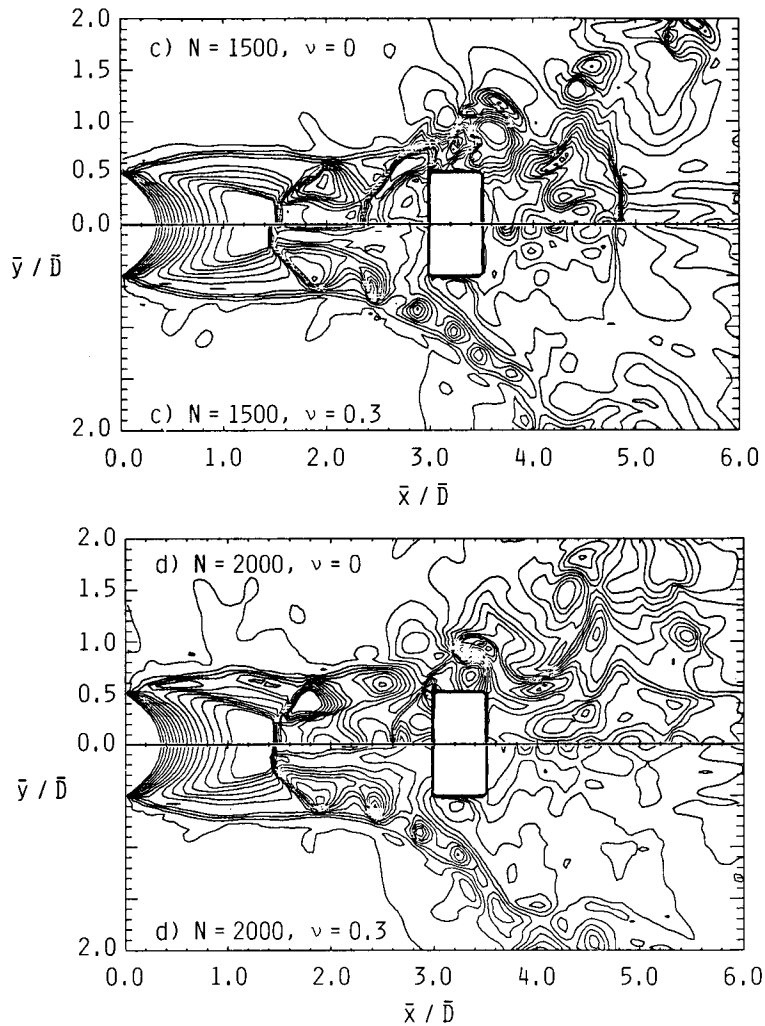


Fig. 9 Comparison of density contours between the one-phase and two-phase cases at a few kinds of time steps.

tribution along the nozzle axis between the one-phase flow (a) and the two-phase one (b) for $20 \leq N \leq 2000$. Note that the dust free result obtained at $N=10000$ is used as the initial condition. Although there is no significant difference in the fluctuating motion of the density of the jet core between the two cases only in the region behind the disk, the fluctuating motion of the density before the disk is suppressed by the presence of particles. This suggests that the presence of particles operates in such a way as to stabilize the flow field. This may be due to the fact that in the dusty jets, interactions between the gas- and

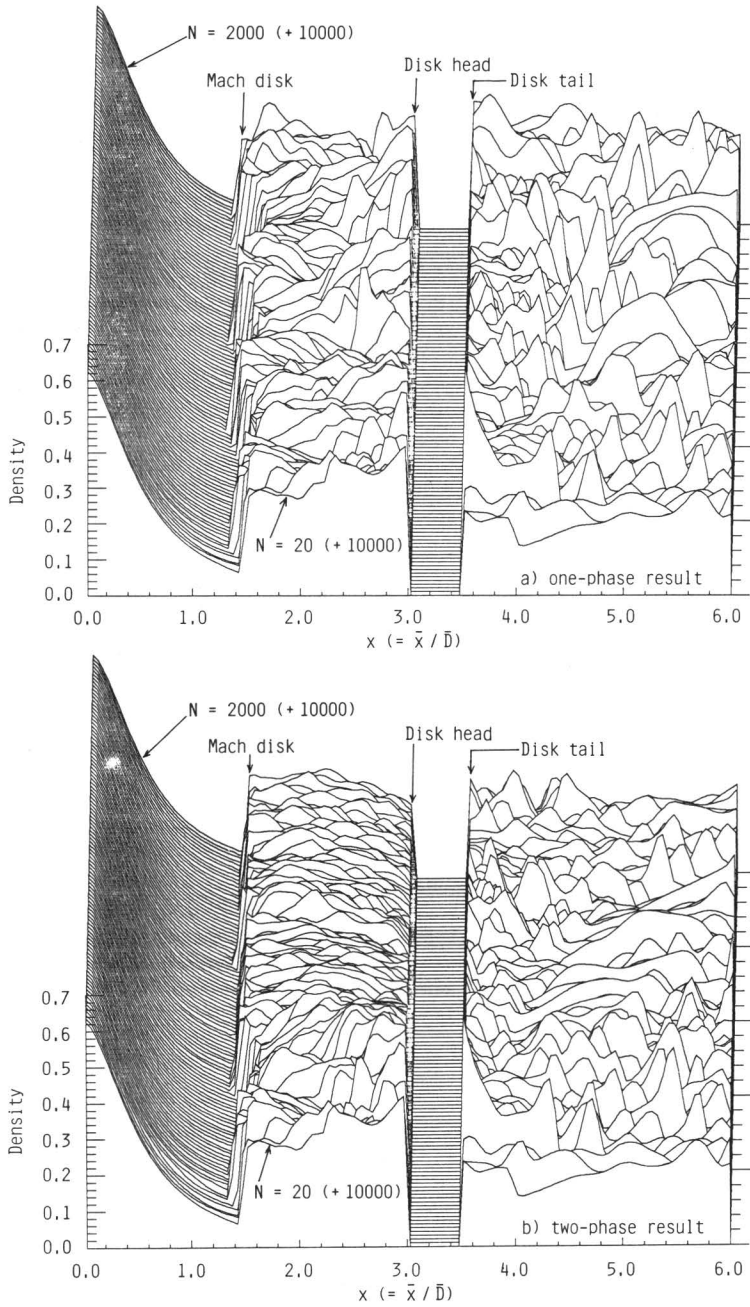


Fig. 10 Time history of density distribution along the jet axis for one-phase flow (a) and two-phase flow (b).

particle-phases tend to suppress the increase in the gas velocity, and the decrease in the gas temperature. In short, a rapid and unstable change in the jet flow field tends to be relieved by the presence of particles.

Figure 11 shows the velocity vectors of particles along the streaklines at several kinds of time steps. What is considered to be interesting here is that the particle cloud is divided into two groups: One group is the particle cloud impinging on the disk and elastically reflecting from it. The other is the particle cloud passing through and around the outer side of the disk. We find from Figure 11 that the particles impinging on the disk near the jet axis experience a few collisions with the body surface, before they flow out of the jet boundary. The number of collisions that a particle experiences depends upon the first impinging location of the particle.

Figure 12 indicates the comparison of the velocity vector field of the two-phase flow with that of the one-phase flow at $N=2000$. First, the effect of the presence of particles on the flow field is seen to be noticeable at a few points: First, the particle subclouds, which have impinged on the disk, are spread conically (see Figure 11(b)), and introduce the gas-phase in the direction of the particle movements. Second, there is a reverse flow of gas in the region downstream from the disk and the particle motion obeys the gas flow there. Third, although some vortical structures are generated by putting the disk in the flow field, the presence of particles tends to shift the locations of vortical structures and the number of the particle subclouds is commonly dilute at/near the vortices.

4.3 One-phase and two-phase supersonic flows around a spherical body

First, in the present case, it should be noted that the computational domain of the gas-phase flow is different from that of the particle-phase one. In order to obtain the numerical solution of the gas-phase flow, the physical space (x, y) is transformed into a computational one (ξ, η) in the form of

$$\xi = (x^2 + y^2)^{1/2} \quad \text{and} \quad \eta = \tan^{-1} \frac{y}{x} \quad (115)$$

In the present calculations, the flow field of the gas-phase is solved in the computational space (ξ, η) , while the flow field of the particle-phase is treated in the original physical space (x, y) . Figure 13 indicates the physical domain used here (a) and the transformed domain (b). The computational domain for the gas-phase flow to be solved consists of the symmetric axis AB, the outer boundary BC, the downstream boundary CD and the inner boundary DA corre-

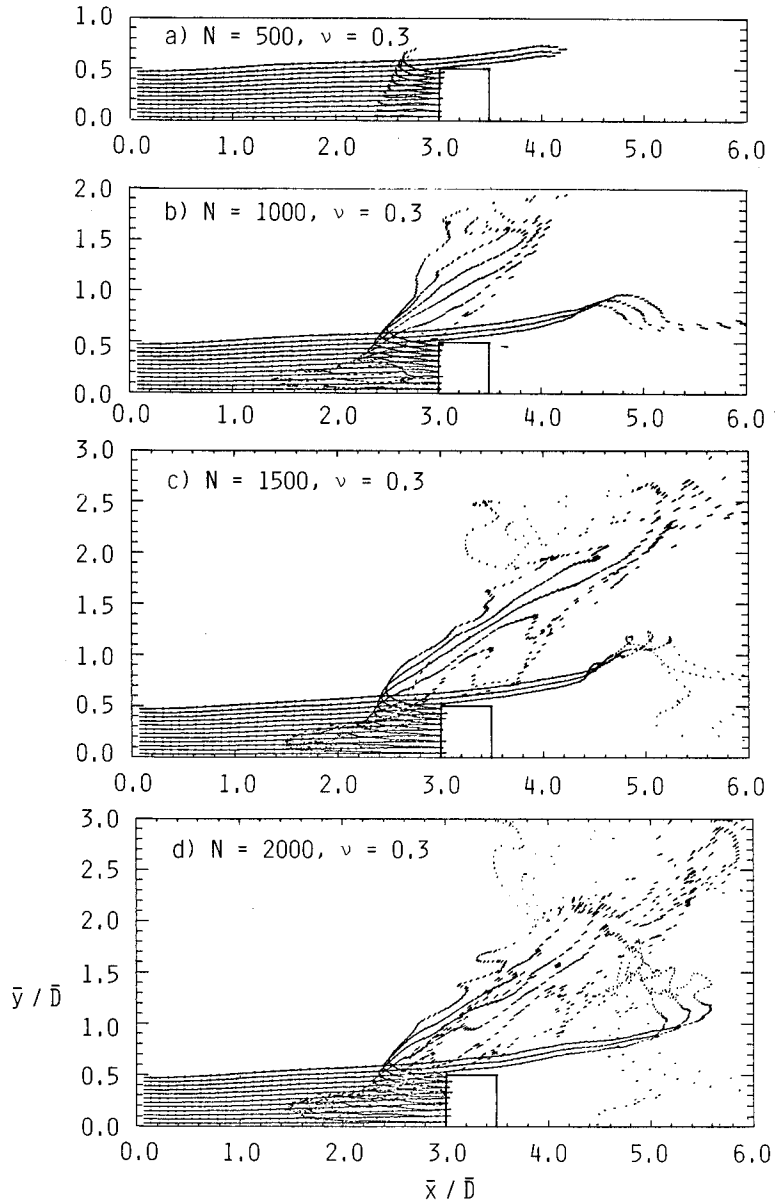


Fig. 11 Velocity vectors of particles along streaklines at several kinds of time steps.

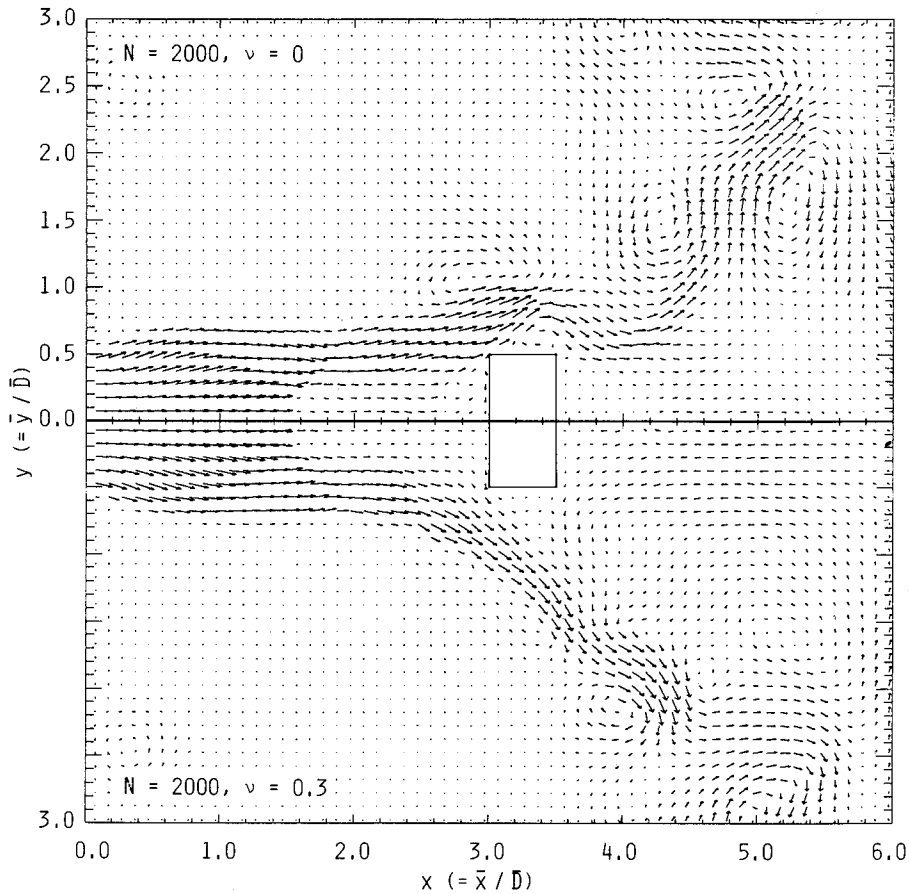


Fig. 12 Comparison of velocity vector field of two-phase flow with that of one-phase flow at $N=2000$.

sponding to the sphere surface. This computational domain is divided into 100×100 fan-shaped meshes which are equally cut in the radial and tangential directions.

Therefore, the transformation of the (x, y) coordinate system to the (ξ, η) system needs to be performed according to the prescription mentioned in section 3.2. Eq. (115) is equivalent to the relation of $x = \xi \cos \eta$ and $y = \xi \sin \eta$. Thereby, the Jacobian J of the transformation is easily obtained by Eq. (102) as $1/\xi$. So that, the four parameters appearing in Eq. (104) are given by

$$\left. \begin{aligned} m_x &= \xi \cos \eta, & m_y &= \xi \sin \eta \\ n_x &= -\sin \eta, & n_y &= \cos \eta \end{aligned} \right\} \quad (116)$$

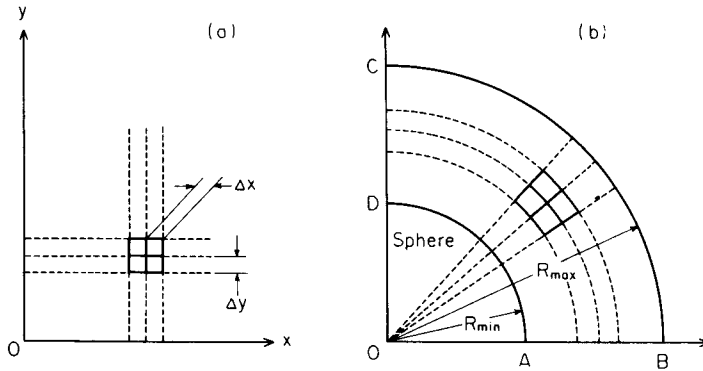


Fig. 13 Computational domain. Note that the flow field of particle-phase is solved in the original physical space (a), while the flow field of gas-phase is done in the transformed space (b).

For the one-phase flows, the dependent variable Q and the fluxes F, G are replaced by \tilde{Q}, \tilde{F} , and \tilde{G} (see Eq. (104)). For the axisymmetric two-phase flows, H and H_p must be transformed into \tilde{H} and \tilde{H}_p , respectively, according to Eq. (106). It is self-evident that the supersonic jet flow around a spherical body to be treated here is axisymmetric. In this sense, the numerical scheme utilized here is first constructed in the cylindrical coordinate system (x, y) . Then it is transformed into the spherical coordinate system (ξ, η) according to the above description.

Particularly for the particle-phase, there is no problem in finding the numerical solutions to the system of equations described in Eqs. (41) and (42) in the cylindrical coordinate system (x, y) .

The boundary conditions of the whole computational domain are constituted by the following. The symmetric condition is applied to the boundaries AB and AD (see Figure 13(a)), and the uniform flow condition on the outer boundary BC. This corresponds to the condition that the additional cells outside of the boundary BC are filled with the gas of the interior cells next to the boundary in a uniform flow state. Also, the outflow condition is applied to the boundary CD. This is the condition that only an outflow from the computational domain to the exterior of the boundary CD is permitted and the opposite flow is not permissible.

Next, we wish to mention the initialization of the flow field in the computational domain. At $t=0$ ($N=0$), the particle subclouds located in front of the sphere are injected into the flow field of a uniform supersonic gas flow over the whole computational domain. The particle subclouds are located uniformly

on a circular plane of r_0 in radius, perpendicular to the symmetric axis at $x=x_0$ ($x_0 > R_{\min}$, R_{\min} ; the radius of the sphere). We divide r_0 of the circular plane equally into K parts and so put the subclouds at the center of each part. In the present situation, we put $r_0 = 1.25$, $x_0 = 1.3$, $R_{\min} = 1.0$ and $R_{\max} = 2.0$ where R_{\max} denotes the distance from the center of the sphere to the outer boundary BC (say, the outer radius of the computational domain). Note that $R_{\max} > (x_0^2 + r_0^2)^{1/2}$. Again, $K = 100$ is used in this calculation. The particles are injected into the flow field at the 100 fixed points on the circular plane at each time step. The state of the uniform gas of $p = 1$ and $\rho = 1$ flowing towards the sphere at the Mach number $M = 3$ (as $v = 0$) is input at all of the centroidal grid points at $t = 0$. Also the particles at the injection points are assumed to be in velocity and thermal equilibrium with the gas.

In the present case, the characteristic length of the flow field \bar{L} is represented by the radius of the sphere ($\bar{R}_{\min} = 3$ cm). The physical constants of the gas and particles adopted are the same as in Table 1. The particle radius is assumed to be $\bar{r}_p = 10 \mu\text{m}$ uniformly and the loading ratio is taken to be $\nu = 0.3$.

Here, one should keep in mind that the time-converged one-phase solution is not used for the calculation of two-phase flows as an initial flow condition. The variation of the flow field from the above mentioned initial state to the steady state with time will be investigated for the two-phase flow.

Although the purpose of this section is to investigate the two-phase flows, it is worthwhile to give a simple description of dust-free (gas-only) flows around a sphere. This is also necessary to check the validity and reliability of the present numerical scheme.

The solutions for various Mach number M have demonstrated a satisfactory time-convergence of the flow field. The profiles of the pressure distribution along the sphere surface have been compared with the theoretical results by Belotserkovskii¹⁷⁾. It has been proved that this agrees well with the experiments. Figure 14 indicates the comparison of our numerical results with the theoretical ones. It follows from this figure that there is an excellent agreement between the two.

Figure 15 shows the density contours of the one-phase flow around the sphere in the shock layer for $2000 \leq N \leq 10000$ at every 2000 time steps. First, we can remark that the one-phase flows around the sphere are fairly stable and the bow shock tends to shift towards the sphere only in the early stage. Next, the flow field in the shock layer behind the bow shock can be said to become steady and stable in a relatively early period.

Figure 16 shows the distribution of the velocity vectors of the gas flow over

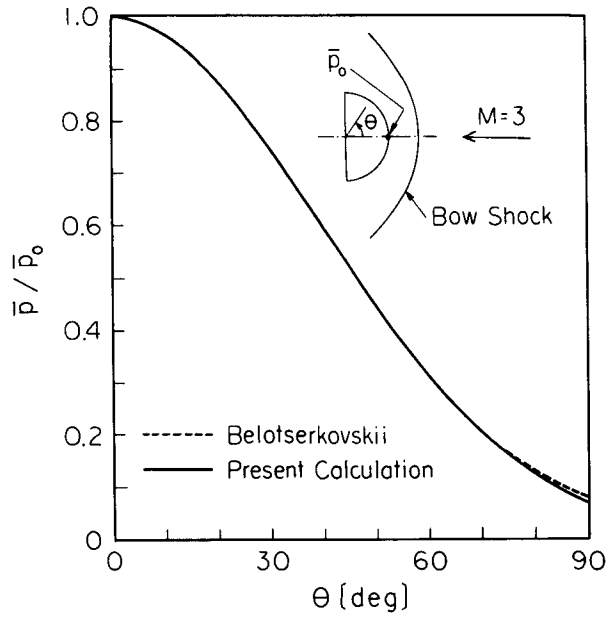


Fig. 14 Comparison of numerical results with theoretical ones by Belotserkovskii.

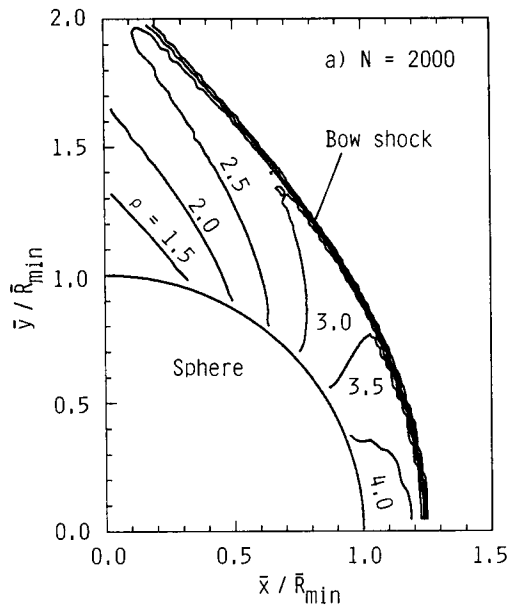


Fig. 15 For caption see next page.

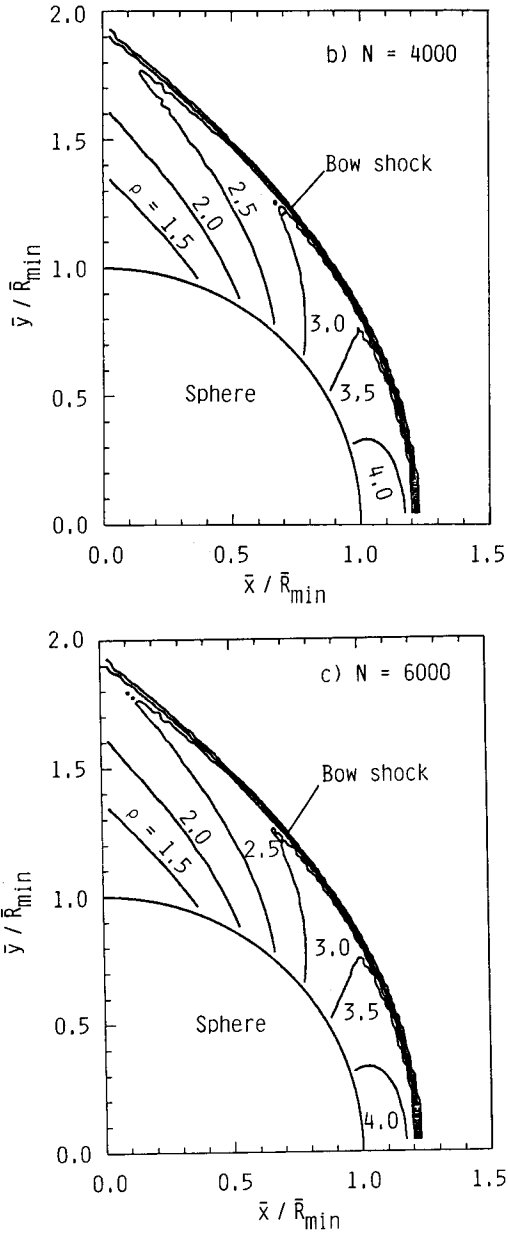


Fig. 15 For caption see next page.

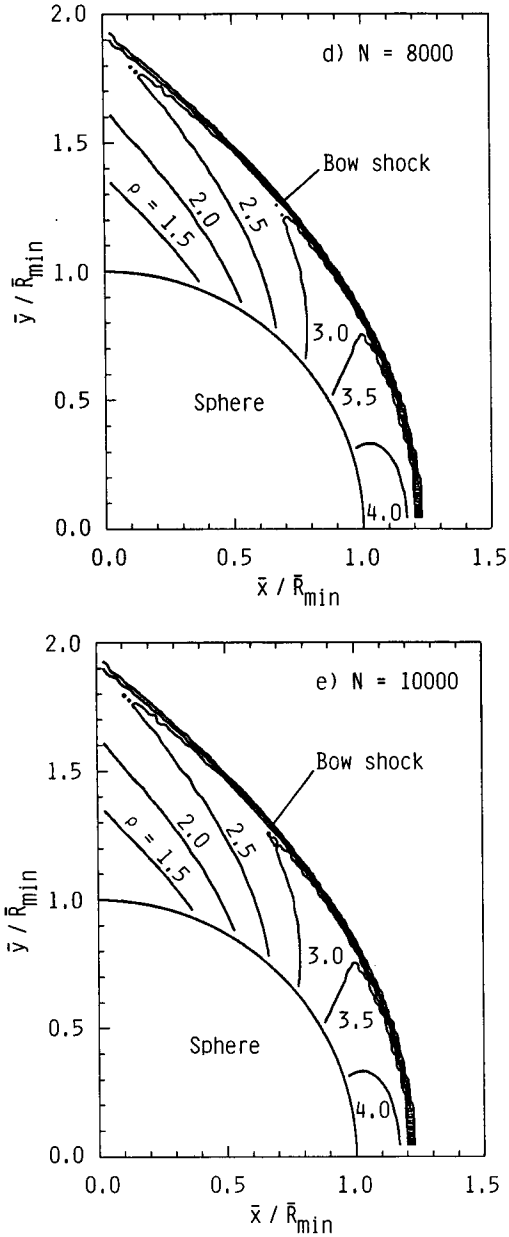


Fig. 15 Density contour of one-phase flow around a sphere in the shock layer for $2000 \leq N \leq 10000$ at every 2000 time steps.

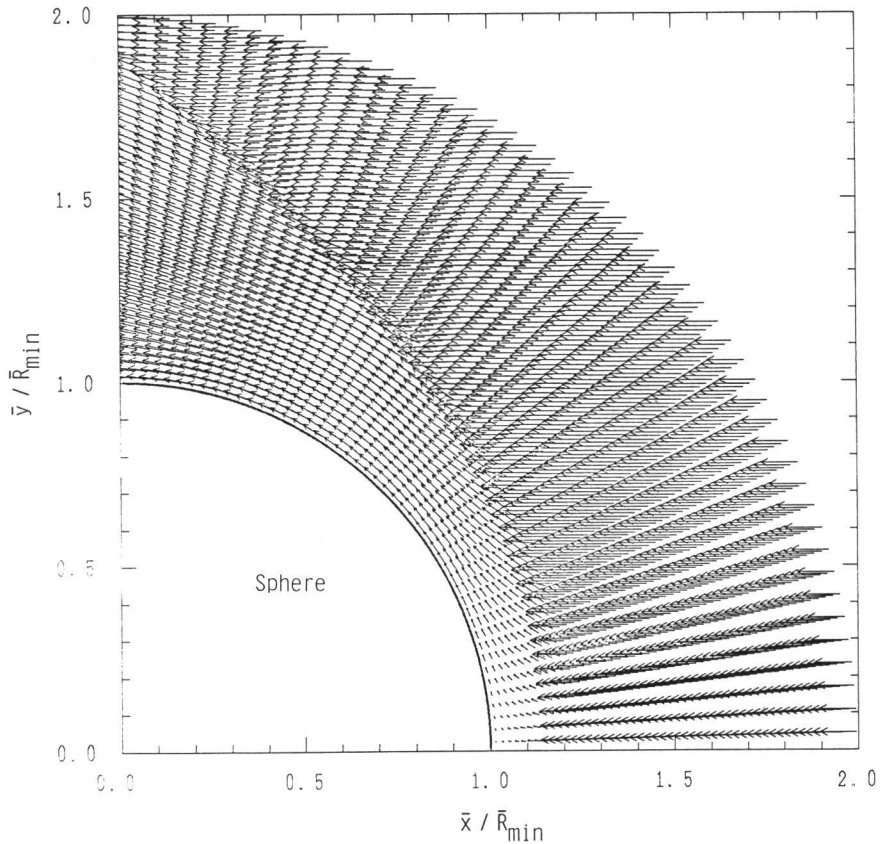


Fig. 16 Field of velocity vectors of one-phase flow over whole computational domain at $N=10000$.

the whole computational domain at $N=10000$. Outside of the bow shock, the velocity vector has no tangential component. Also, the velocity is accelerated along the sphere surface from the stagnation point to the top of the spherical body and is increased in magnitude at a larger radial distance from the sphere surface in the shock layer.

Next, for the one-phase flow we wish to demonstrate the variation of the gas density along the body axis as well as on the sphere surface from the stagnation point to the top of the sphere with time. Figure 17 shows the time history of the density for $40 \leq N \leq 4000$ at every 40 time steps. The bow shock existing almost in contact with the sphere surface in the initial flow field tends to shift the location towards the upstream side with time, and then the location of the bow shock is fixed at $N=2000$ or so. In addition, weakly fluctuating waves, which are observed just behind the bow shock still beyond $N=2000$, are annihilated

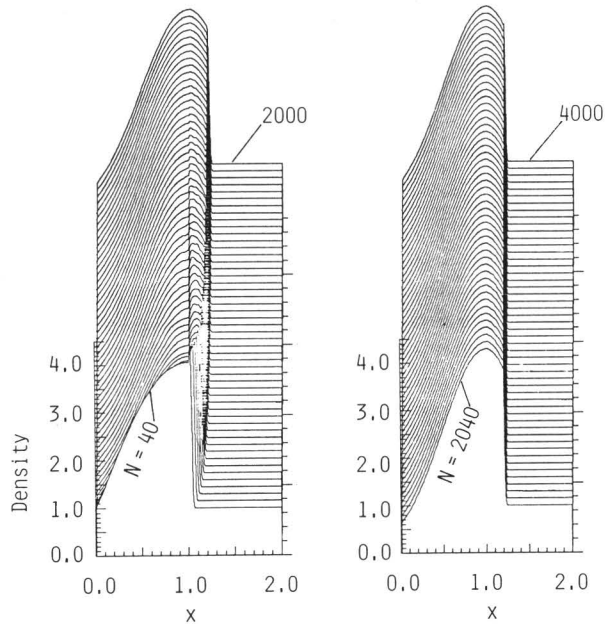


Fig. 17 Time history of density along body axis for $40 \leq N \leq 4000$ at every 40 time steps.

perfectly at $N = 4000$. This suggests that for one-phase flows around a sphere a time-converged solution may be obtained beyond $N = 4000$.

Here, we show the numerical results of the two-phase flow around a sphere. Figure 18 indicates the contour of the constant gas density (a), the field of the velocity vectors of gas (b) and that of particles along the streaklines (c) at $N = 3000, 4000, 5000, 6000, 7000$ and 12000 . Here, one should bear in mind that the field of velocity vectors shown in Figure 18(c) is not along the trajectories of particular particles, but along the streaklines consisting of all of the injected particles according to the time series. The most important problem is to investigate whether or not the steady and stable flow field can be reached as N is infinitely increased. Comparing the density contour of this case with that of the single-phase result (see Figure 15), the former seems to be very unsteady, especially, in the stagnating region in the neighbourhood of the body axis in the shock layer even for the large time step N . The unsteady numerical result can also be accepted obviously from the field of the velocity vectors along the streaklines of particles. If the condition that the particles stick or are absorbed perfectly inelastically to the body surface is imposed on the numerical simulations, as soon as particles impinge on the body surface, the time-converged

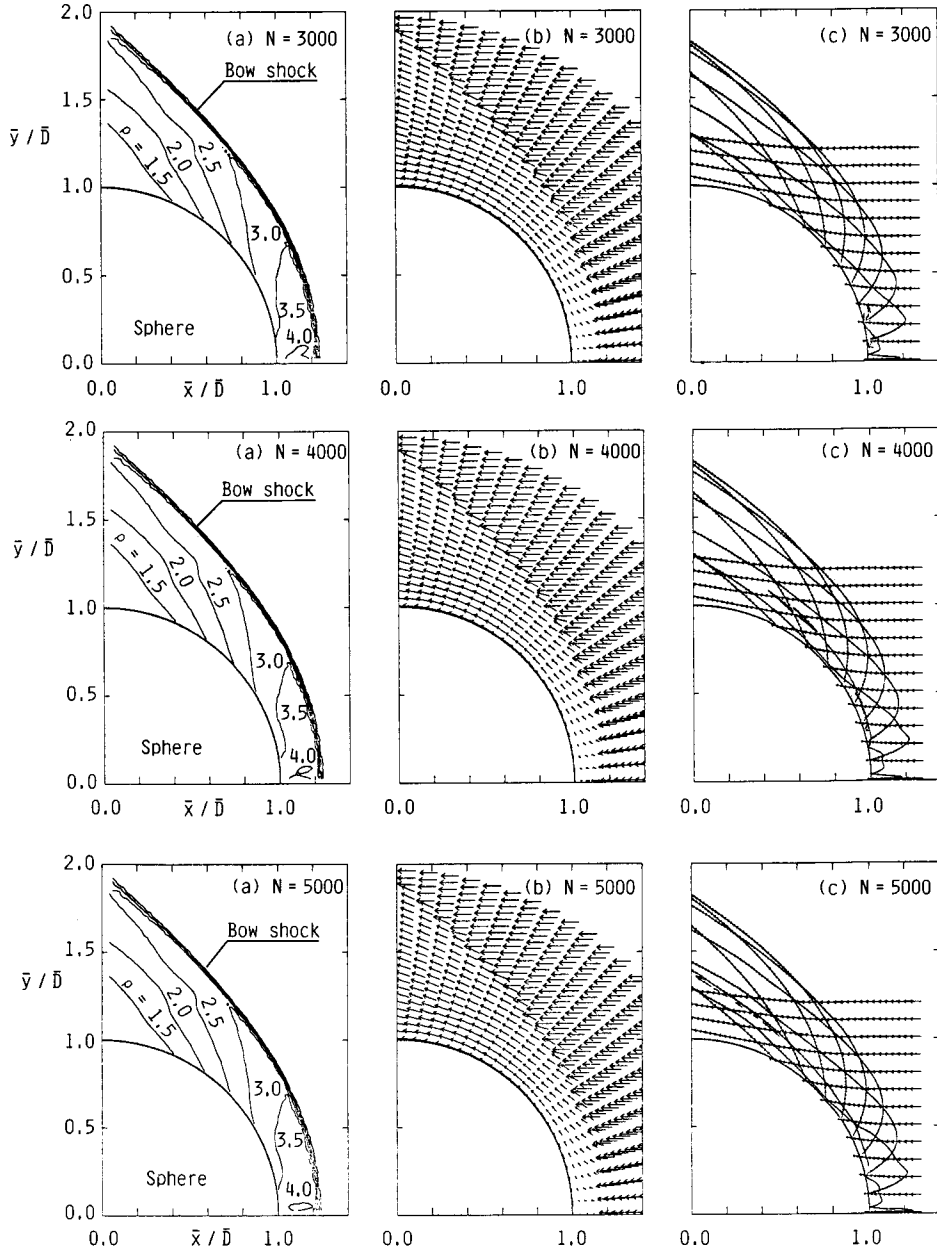


Fig. 18 For caption see next page.

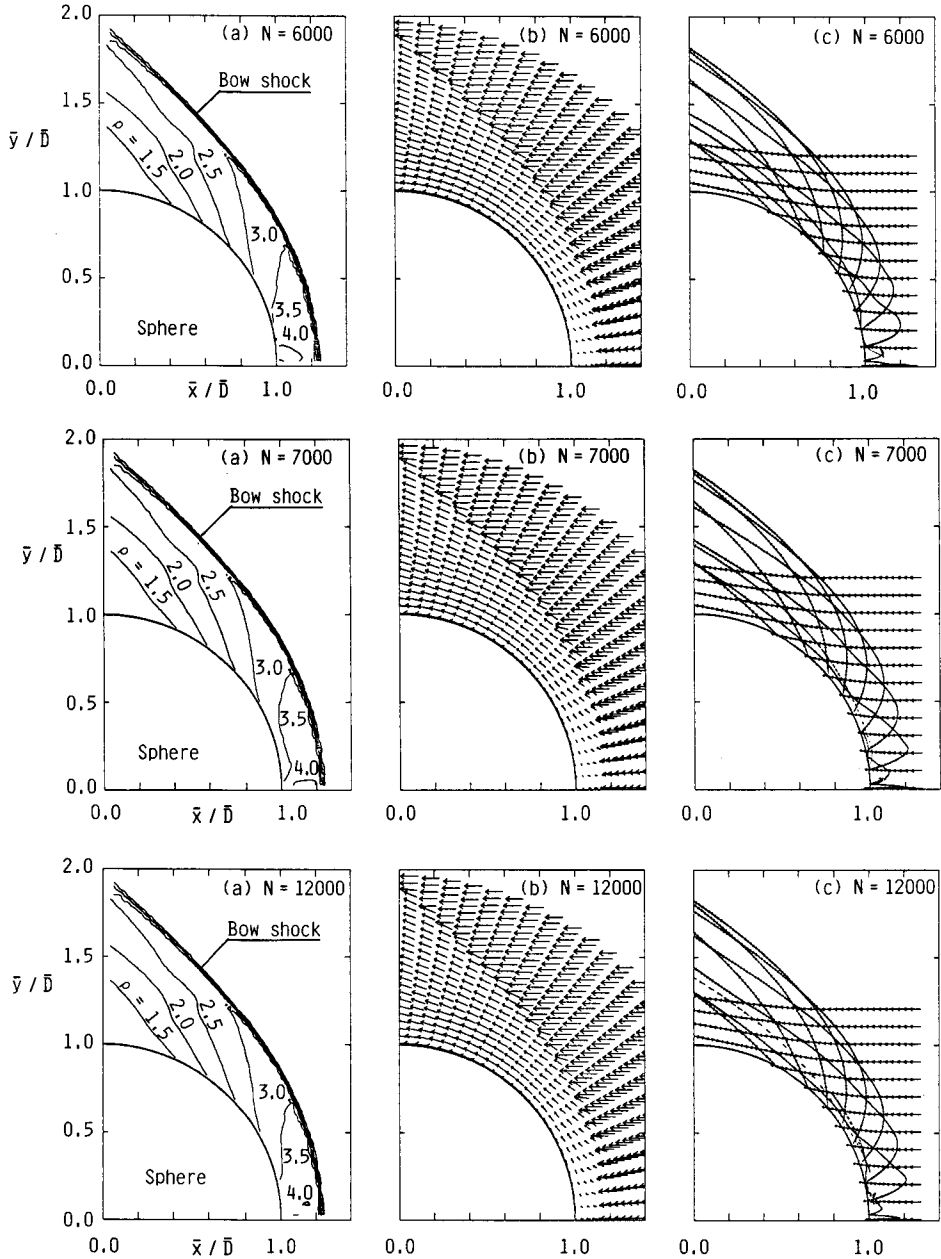


Fig. 18 Indications of contour of constant gas density (a), field of gas velocity vectors (b) and field of velocity vectors of particles (c) for two-phase flow at several kinds of time steps.

solutions must presumably be obtained¹⁹⁾. The present situation is different entirely from the foregoing case. On the assumption that the particles that impinge on the body surface are reflected perfectly elastically, the present numerical simulations have been performed, as has been mentioned already. Also, it is assumed that only the velocity component normal to the body surface is reversed and the tangential component remains unvaried on the reflection condition: The so-called specular reflection is conditioned.

Practically, the particles that must impinge on the body surface are decelerated by the gas in the shock layer and then reflected from the surface with a finite velocity. The particles impinging on the surface near the body axis experience a few elastic collisions with the sphere. The streaklines of particles, shown in Figure 18(c), are taken at 8 intervals of injection points including the first streakline of particles injected from the point next to the body axis. For a closer investigation, we consider the behavior of particles along the first streakline for example. The particles impinging almost normally to the sphere surface are reflected also normally to it. The normal component of the velocity of the reflected particles decreases owing to the reverse flow of the gas and is missing somewhere. The particles are again moved downstream by the gas flow and the second impingement of the particles on the surface occurs. However, the velocity of the particles reflected from the sphere can be considered to be small in magnitude. At the same time, these particles move only in an almost stagnant state near the sphere surface where the gas velocity also is small in magnitude, until the particles flow out of the stagnant region. As a result, it can be expected that the number density of the particles is increased near the body axis, and that the number density is distributed densely upstream and dilutely downstream along the sphere surface, as will be discussed later. Furthermore, the distribution of the number density does not remain unchanged even for the large time step N .

The above mentioned tendency becomes weaker for the particles along the streaklines injected at positions farther from the body axis (see Figure 18(c)). Again, what is noticeable as another problem is that the particles rebounded from the sphere surface do not break the bow shock at all, at least, in the present situation.

We wish to demonstrate the instability of the flow field near the body axis in the shock layer from a different point of view. Figure 19 indicates the time history of the density for the two-phase flow, corresponding to Figure 17, for $5040 \leq N \leq 12000$ at very 40 time steps. Obviously, the density field in the shock layer is unstable and unsteady. There also seems to be no periodicity in the

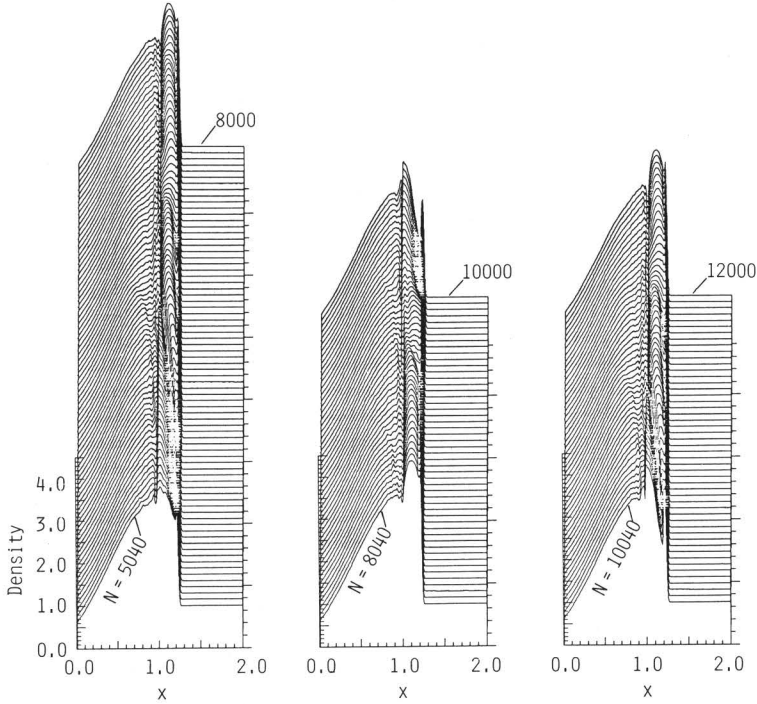


Fig. 19 Time history of density for two-phase flow corresponding to one-phase flow shown in Fig. 17 for $5040 \leq N \leq 12000$ at every 40 time steps.

unsteady behavior. The so-called stagnation point does not always take the maximum gas density, as encountered in the one-phase flow. Rather, the maximum density is seen to be in the middle part of the shock layer near the body axis, although it is unsteady and unstable. Furthermore, instability is also observed in a relatively small region upstream along the sphere surface near the stagnation point.

5. Discussion and conclusion

Up to this point, we have demonstrated very interesting numerical results for the various flow fields of the one-phase and two-phase cases, which have been obtained by the Osher scheme.

First, we discuss the truncation error of the scheme in the form obtained by replacing the \tilde{dF} and $\tilde{\tilde{dF}}$ terms that occur in Eq. (89) with their corresponding unlimited dF values (see Eq. (88)).

Combining Eqs. (61) and (62) to Eq. (88), we have

$$\begin{aligned} \bar{F}_{j+1/2} - \bar{F}_{j-1/2} &= \frac{\eta-1}{4} dF_{j+3/2}^- + \frac{1+\eta}{4} dF_{j+1/2}^+ + \frac{4-2\eta}{4} dF_{j+1/2}^- \\ &+ \frac{4-2\eta}{4} dF_{j-1/2}^+ + \frac{1+\eta}{4} dF_{j-1/2}^- + \frac{\eta-1}{4} dF_{j-3/2}^+ \end{aligned} \quad (117)$$

By the Taylor expansion,

$$F_{j+3/2} = F_j + \frac{3}{2} \Delta x \left(\frac{\partial F}{\partial x} \right)_j + \frac{1}{2} \left(\frac{3\Delta x}{2} \right)^2 \left(\frac{\partial^2 F}{\partial x^2} \right)_j + \frac{1}{6} \left(\frac{3\Delta x}{2} \right)^3 \left(\frac{\partial^3 F}{\partial x^3} \right)_j + O((\Delta x)^4)$$

and

$$F_{j+1} = F_j + \Delta x \left(\frac{\partial F}{\partial x} \right)_j + \frac{1}{2} (\Delta x)^2 \left(\frac{\partial^2 F}{\partial x^2} \right)_j + \frac{1}{6} (\Delta x)^3 \left(\frac{\partial^3 F}{\partial x^3} \right)_j + O((\Delta x)^4)$$

so that

$$dF_{j+3/2}^- = \frac{\Delta x}{2} \left(\frac{\partial F}{\partial x} \right)_j + \frac{5}{8} (\Delta x)^2 \left(\frac{\partial^2 F}{\partial x^2} \right)_j + \frac{19}{48} (\Delta x)^3 \left(\frac{\partial^3 F}{\partial x^3} \right)_j + O((\Delta x)^4) \quad (118)$$

Similarly,

$$dF_{j+1/2}^+ = \frac{\Delta x}{2} \left(\frac{\partial F}{\partial x} \right)_j + \frac{3}{8} (\Delta x)^2 \left(\frac{\partial^2 F}{\partial x^2} \right)_j + \frac{7}{48} (\Delta x)^3 \left(\frac{\partial^3 F}{\partial x^3} \right)_j + O((\Delta x)^4) \quad (119)$$

$$dF_{j+1/2}^- = \frac{\Delta x}{2} \left(\frac{\partial F}{\partial x} \right)_j + \frac{1}{8} (\Delta x)^2 \left(\frac{\partial^2 F}{\partial x^2} \right)_j + \frac{1}{48} (\Delta x)^3 \left(\frac{\partial^3 F}{\partial x^3} \right)_j + O((\Delta x)^4) \quad (120)$$

$$dF_{j-1/2}^+ = \frac{\Delta x}{2} \left(\frac{\partial F}{\partial x} \right)_j - \frac{1}{8} (\Delta x)^2 \left(\frac{\partial^2 F}{\partial x^2} \right)_j + \frac{1}{48} (\Delta x)^3 \left(\frac{\partial^3 F}{\partial x^3} \right)_j + O((\Delta x)^4) \quad (121)$$

$$dF_{j-1/2}^- = \frac{\Delta x}{2} \left(\frac{\partial F}{\partial x} \right)_j - \frac{3}{8} (\Delta x)^2 \left(\frac{\partial^2 F}{\partial x^2} \right)_j + \frac{7}{48} (\Delta x)^3 \left(\frac{\partial^3 F}{\partial x^3} \right)_j + O((\Delta x)^4) \quad (122)$$

$$dF_{j-3/2}^+ = \frac{\Delta x}{2} \left(\frac{\partial F}{\partial x} \right)_j - \frac{5}{8} (\Delta x)^2 \left(\frac{\partial^2 F}{\partial x^2} \right)_j + \frac{19}{48} (\Delta x)^3 \left(\frac{\partial^3 F}{\partial x^3} \right)_j + O((\Delta x)^4) \quad (123)$$

Substituting Eqs. (118) to (123) into Eq. (117) and arranging the result, we have

$$\bar{F}_{j+1/2} - \bar{F}_{j-1/2} = \Delta x \left(\frac{\partial F}{\partial x} \right)_j + \frac{(\Delta x)^3}{4} \left(\eta - \frac{1}{3} \right) \left(\frac{\partial^3 F}{\partial x^3} \right)_j + O((\Delta x)^4) \quad (124)$$

or

$$\frac{\bar{F}_{j+1/2} - \bar{F}_{j-1/2}}{\Delta x} = \left(\frac{\partial F}{\partial x} \right)_j - \frac{(\eta-1/3)}{4} (\Delta x)^2 \left(\frac{\partial^3 F}{\partial x^3} \right)_j + O((\Delta x)^3) \quad (125)$$

Therefore, the truncation error of the unlimited forms is given by the second

term in the right hand side of the above equation. It is interesting to note that the truncation error is independent of the particular upwind-scheme used, that is, independent of \tilde{F} . Furthermore, it should be added that $\eta = 1/3$ has been selected throughout this paper, and therefore all of the present calculations have been performed by the third-order accurate scheme.

We discuss the numerical results of the free jets for the one-phase and two-phase cases as a very simple flow field. Although we have found that the single-phase results agree well with the experimental ones, in particular, for the characteristics of the first shock-cell structure, the flow field downstream from the Mach disk is observed to be fluctuating and oscillatory even for the large N , as shown in Figure 4. When the pressure ratio, p_0/p_∞ , is taken to be small, the variation of the propagating process of discontinuous and continuous waves with time can not clearly be emphasized, as observed in Figures 4(a) and 7. Hence, the time histories of the density distribution along the jet axis calculated under the condition that $p_0/p_\infty = 5.8$ are shown for $2001 \leq N \leq 2100$ at every time step in Figure 20. For both the one-phase flow (a) and the two-phase one (b), the gas density distribution in the region downstream from the Mach disk is observed to change in such a manner as to propagate the nearly periodically appearing waves towards the downstream boundary.

Figure 21 gives the comparison of the time history of the density distribution along the nozzle axis between the one-phase flow (a) and the two-phase one (b) for $2001 \leq N \leq 2100$ at every time step, when the disk normal to the jet axis stands in the flow field. For the one-phase flow, there is observed a dome-shaped shock in front of the disk (see Figure 9) besides the normal shock at the Mach disk. At least, the pressure jump occurs there and the shock wave can be confirmed also from Figure 9. The most prominent feature is the strong oscillating shock wave between the Mach disk and the circular plate (disk). The shock wave oscillates through a large amplitude, on the axis equal to about $0.25 \bar{D}$, about a mean standoff distance $s = 0.5 \bar{D}$ from the disk. Thus, such an unstable flow field agrees fairly well with the experimental results by Powell¹⁸⁾. In the region downstream from the disk, there are density waves propagating downstream and upstream, and the variation of the density distribution with time is somewhat periodic.

Next, for the two-phase flow, the flow field in the region upstream from the disk normal to the jet axis is apparently more stable in comparison with the one-phase result. The most prominent feature is that there is no shock wave in front of the disk which can be evidently present in the one-phase flow field. Therefore, the density field is very stable between the Mach disk and the plate

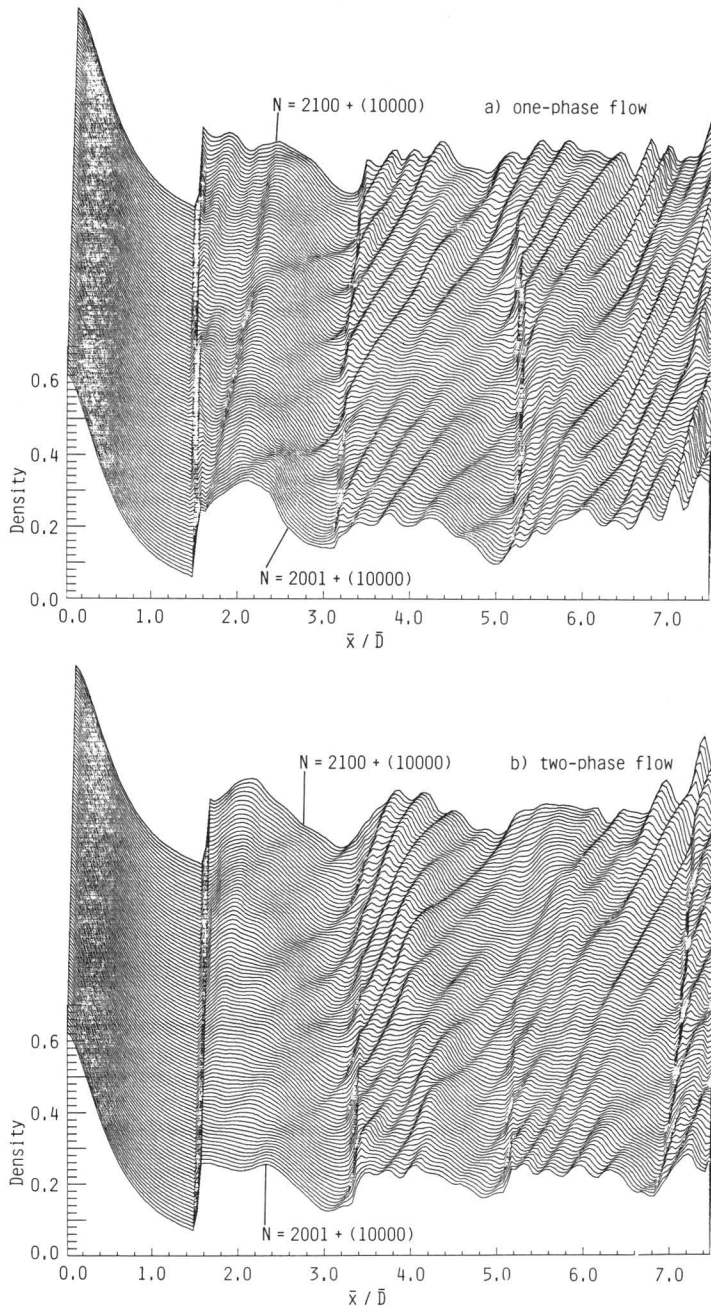


Fig. 20 Time history of density distribution along jet axis calculated under condition that $\bar{p}_0/\bar{p}_\infty=5.8$ for $2001 \leq N \leq 2100$ at every time step: One-phase flow (a) and two-phase flow (b).

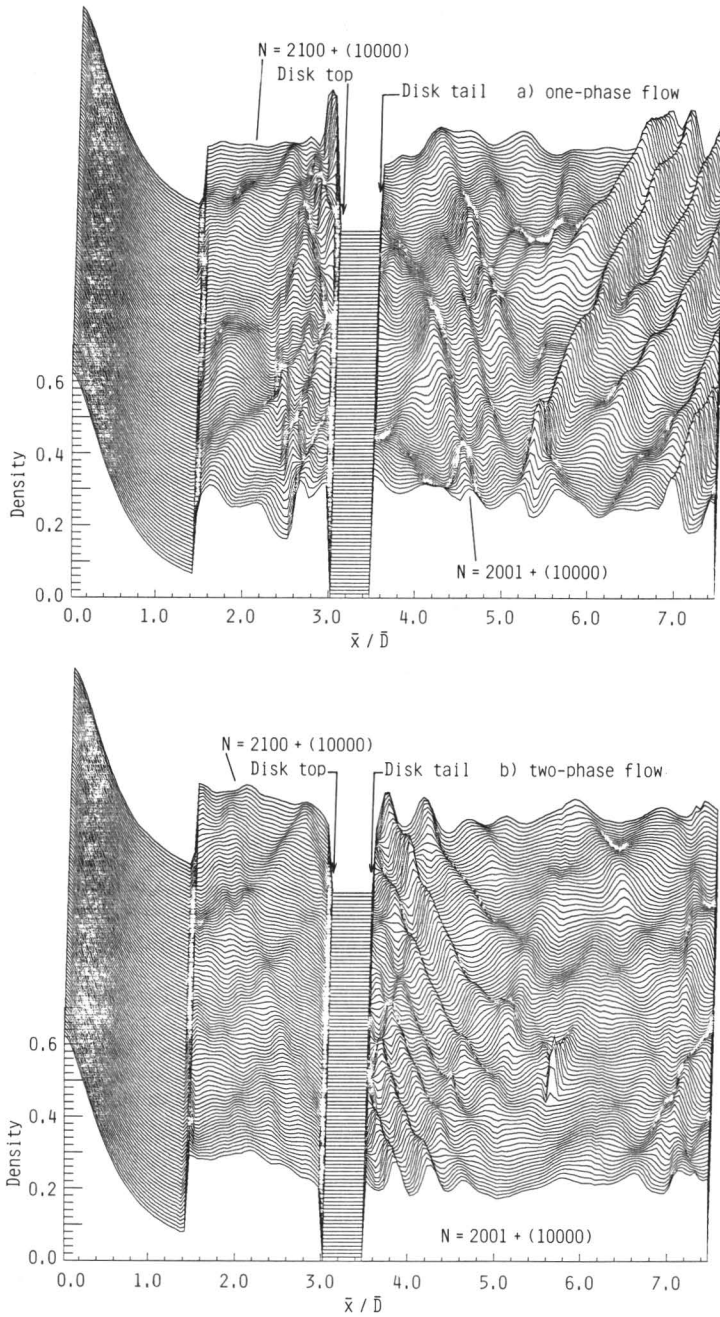


Fig. 21 Time history of density distribution along jet axis for one-phase flow (a) and two-phase flow (b) interacting with a disk normal to jet axis.

owing to the presence of particles leading to the annihilation of the above mentioned dome-shaped shock wave. In the region downstream from the disk tail, a nearly periodically occurring wave is observed to propagate towards the disk tail. Again a local disturbance of the density observed at $x(=\bar{x}/\bar{D}) \simeq 5.6$ in Figure 21(b) seems to be due to the access of the particle subcloud to the nozzle axis.

Next, we discuss the effect of the loading ratio ν on the flow field. We consider the case where the particle subclouds are injected into the one-phase flow field obtained at $N=10000$. The computational conditions are the same as in section 4.2, except that $\nu=1.0$. Figure 22 indicates the density contour of the gas-phase (a) and the velocity vectors of the particles along the streaklines (b) at $N=1500$. Comparing the case of $\nu=1$ with that of $\nu=0.3$ (see Figure 9(c)), the predominant feature is that the jet boundary of the flow field is very unclear in the region downstream from the Mach disk for $\nu=1$. On the contrary, the increase in ν tends to make the flight record of the subcloud injected at each position distinct, although there is a slightly unstable oscillatory motion of particles impinging on the disk surface. Presumably the basis that the particle-motion is more stable for $\nu=1.0$ than for $\nu=0.3$ may be due to the inertia effect (or mass effect). Further details concerning the effect of ν on the flow field will be reported elsewhere.

Now, we wish to give a closer consideration to the problem of the two-phase flow around a sphere. As has been pointed out already, the instability in the particle motion is observed to be present in a region near the body axis in the shock layer. Figure 23 indicates the distribution of particle subclouds injected at each time step in such a region at $N=5000$, 7000 and 12000 . It should be remarked in this figure that one particle cloud is represented by one point, and that therefore the points marked by a dot overlap and seem like a darker line in the region where the particle velocity becomes smaller. Although all of the particles contained in the figure region impinge on the sphere surface, the distribution of particles injected near the body axis becomes complicated after the impingement. Also, the region concerned seems to stagnate by the aggregation of the injected and rebounded particles. Figure 24 exhibits the distribution of the number of particle subclouds around the sphere surface in the shock layer at $N=5000$, 7000 and 12000 . We note that the value proportional to the number of particle clouds contained in each fan-shaped mesh which are divided by its area is here taken instead of the number density. As can be expected, the number density is distributed densely in the upstream region and dilutely in the downstream along the sphere in the shock layer. Again, the distribution does

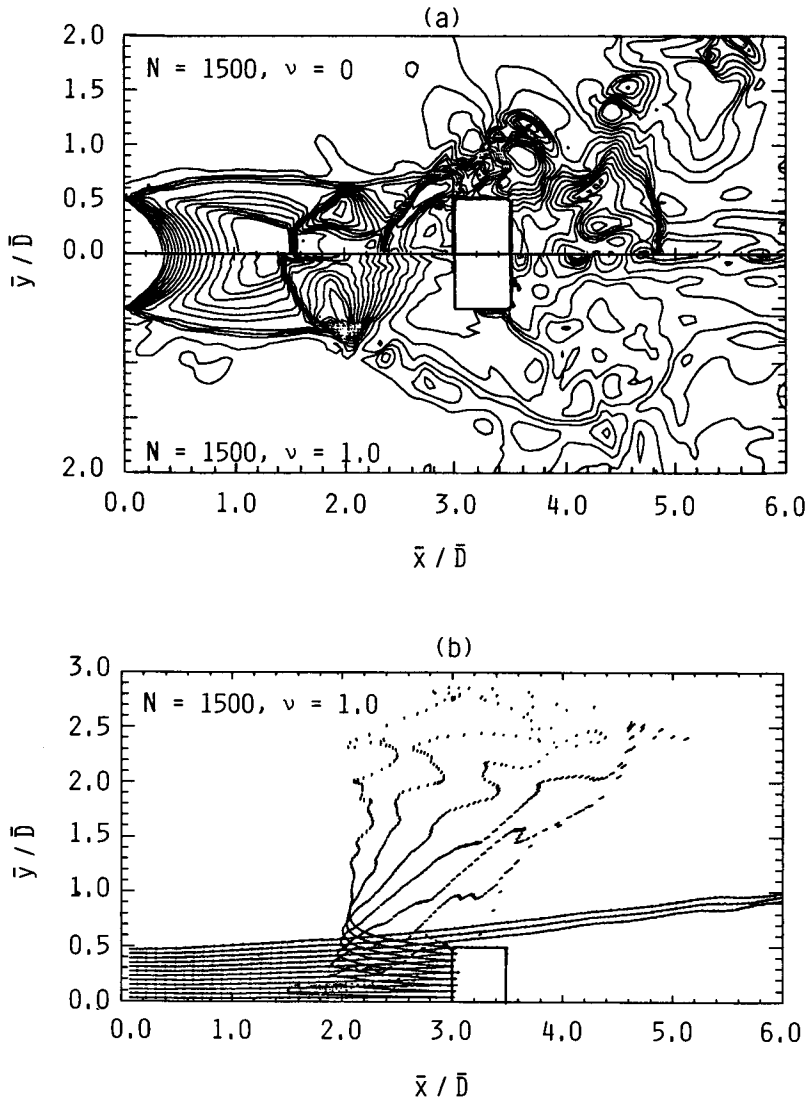


Fig. 22 Density contour of gas-phase (a) and field of velocity vectors of particles along streaklines (b) at $N=1500$. Compare the present case of $\nu=1$ with that of $\nu=0.3$ shown in Fig. 9 (c) and 11 (c).

not always remain unchanged and steady, in particular, in the upstream region. In short, the flow field of particles is unsteady as well as unstable.

Figure 25 indicates the velocity vectors of particles along the streakline injected at the position next to the body axis at $N=12000$. The particles are

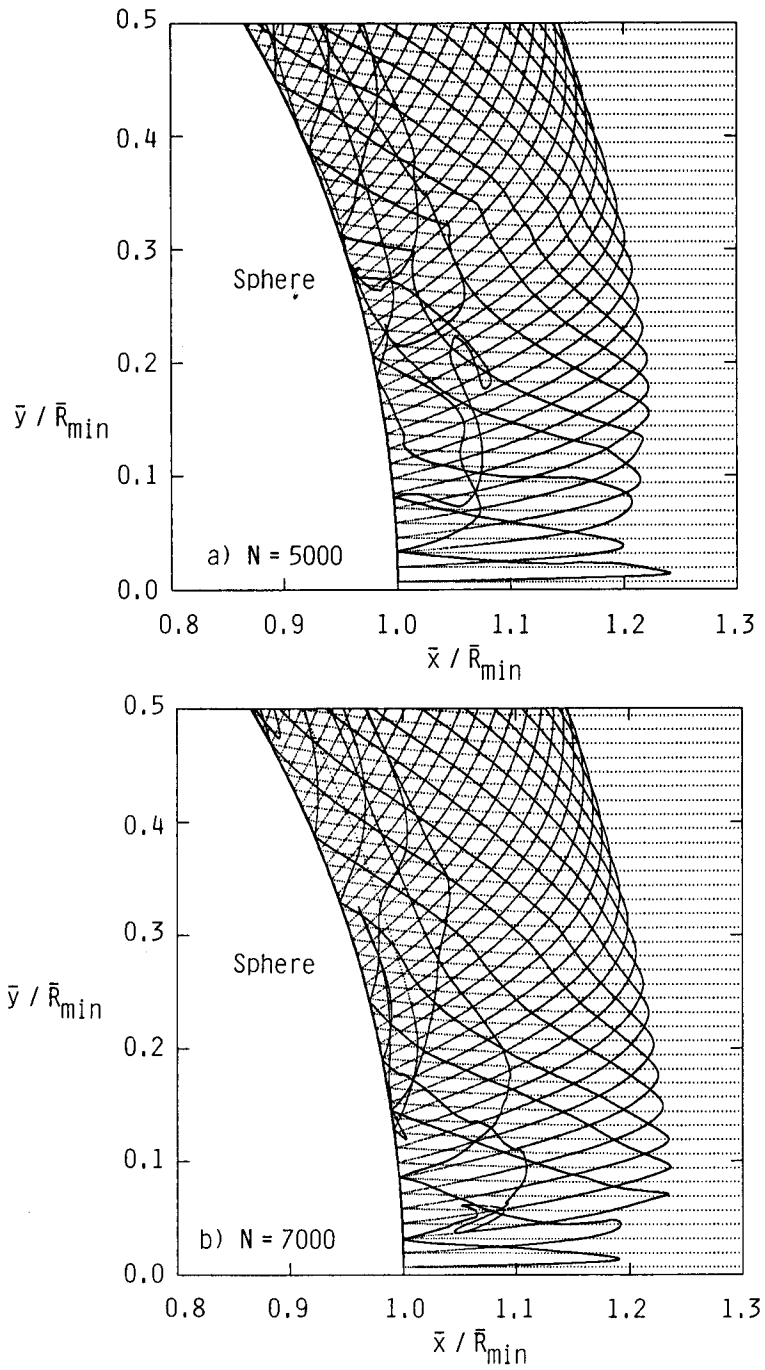


Fig. 23 For caption see next page.

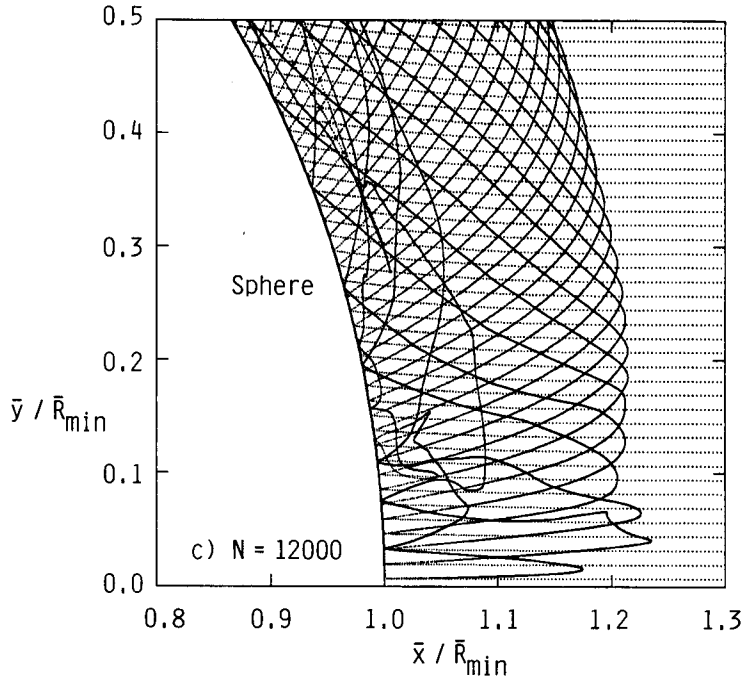


Fig. 23 Distribution of particle subclouds along streaklines in the region upstream along sphere surface at $N=5000, 7000$ and 12000 .

selected at ten times the interval of time step Δt . The velocity of particles reflected from the sphere is considerably small in magnitude in comparison with the case of the first impingement. Again, the first streakline does not exhibit the expected pattern, especially after the second impingement of the particles on the sphere. In addition, the impinging points are understood to be varied with time by comparing each velocity vector direction with the streakline combining particle positions according to the time series (see Figure in Figure 25). The one remaining problem is whether or not the time-converged solution can be reached as $N \rightarrow \infty$.

In fact, the numerical simulation of the supersonic two-phase mixture flow takes a prohibitively long computing time. The reason is because a very large number of particle subclouds injected at the interval of Δt must be followed separately. As a result, the amount of computation increases to an extraordinary degree. We wish to add that the VP rate in our computer program is approximately 0.999, and that the computing time per 5000 time steps takes nearly 10000 sec. At least, at the present stage, it has to be stressed that the two-phase

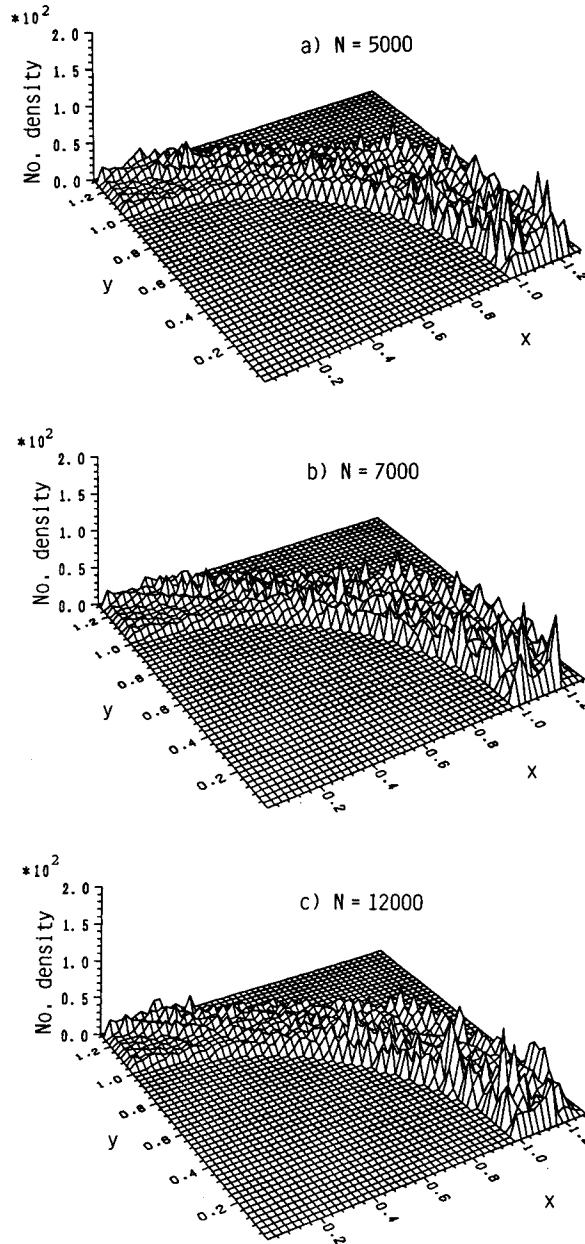


Fig. 24 Distribution of number of particle subclouds around sphere surface in shock layer at $N=5000$, 7000 and 12000 .

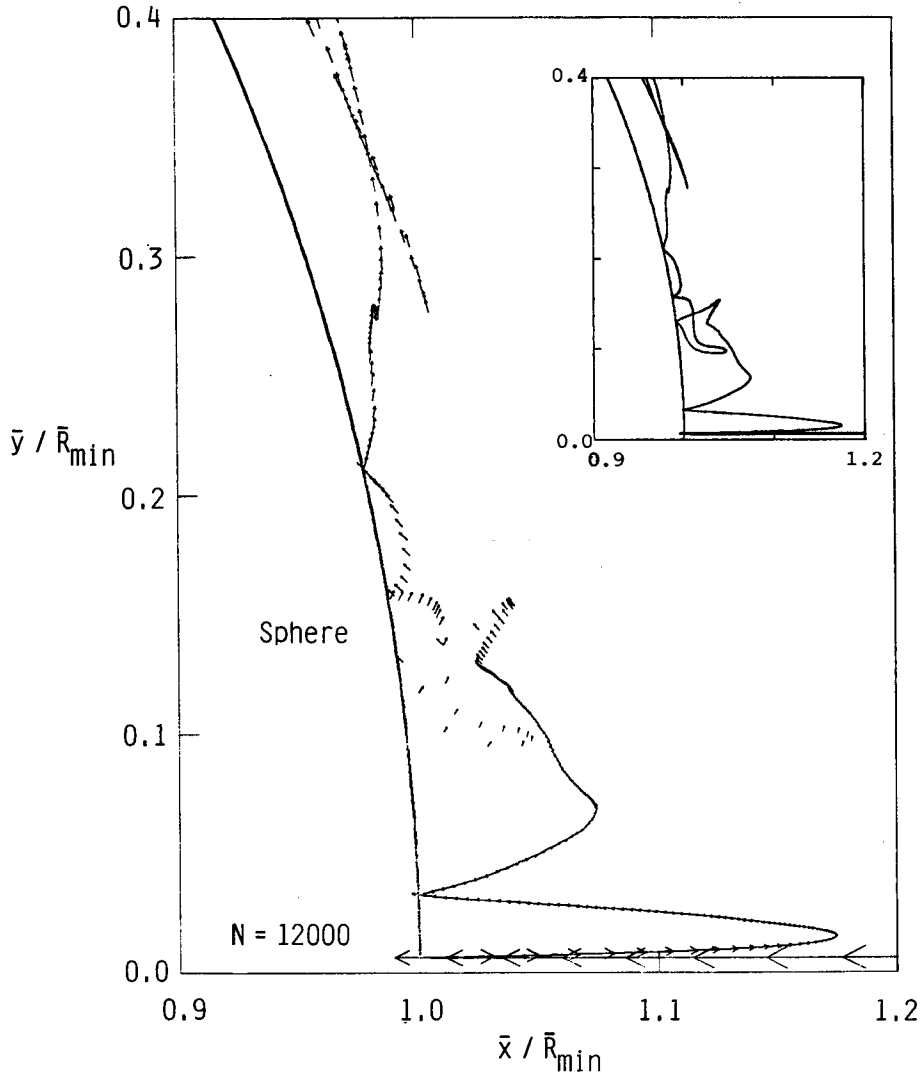


Fig. 25 Velocity vectors along the first streakline of particles injected at the position next to body axis at $N=12000$.

results are not always sufficiently time-converged even for a large number of time steps N due to the discrete treatment of the particle-phase, if we assume $N = 12000$ to be a very large time step. At any rate, we think that it is necessary to solve the problem whether or not the time-converged solutions exist near the stagnation region.

In closing, we reflect that a few important problems to be clarified in the

near future remain left for the supersonic gas-particle two-phase flows.

First, for the flow fields of one-phase jets impinging on a disk perpendicular to the jet axis, the instability should be pursued focusing upon the pressure ratio, the disk size and the disk position. We intend to investigate in detail the change in the position of the Mach disk as well as the behavior of another strong oscillating shock wave existing between the Mach disk and the circular plate (disk) by comparing the numerical results obtained with the experimental ones. For the two-phase flows, we wish to clarify the effect of the presence of particles on the flow field for the two cases where the circular plate is present and absent. These numerical simulations will be performed by varying the mass loading ratio, the Mach number at the nozzle exit, the pressure ratio, the particle size, the size of the circular plate etc. as parameters. Also, we will simulate, from a more realistic point of view, the flow fields of two-phase flows in a free jet region as a perturbation from a non-equilibrium gas-liquid particle mixture flow at the nozzle exit. In this case, a system of equations governing the steady quasi-one-dimensional nozzle flow of a gas-particle mixture is treated on the basis of our previous investigations^{2)~4), 20)}.

Second, for the two-phase flow around a sphere we intend to pursue the process of the instability in the particle motion near the stagnation region for N as large as possible. We consider that there are many factors leading to the instability in the particle motion. For example, when the particle size is very small, the rebounding distance after the impingement of particles on the body surface may presumably be very slight owing to decreasing the inertia effect. In an extreme case the particles may be imagined to move closely along the sphere surface. At any rate, we wish to clarify the basis of the instability in the motion of particles injected at points nearer the body axis in the near future.

Acknowledgment

The authors would like to note that this study has been supported through the Grant in Aid for Scientific Research (01550532) of the Ministry of Education, Science and Culture in Japan.

References

- 1) M.J.Zucrow and J.D.Hoffman: Gas dynamics, II, John Wiley and Sons, New York,

- (1977), p. 53.
- 2) N. Hatta, R. Ishii, H. Takuda, K. Ueda and J. Kokado: *Trans. ISIJ*, 28 (1988), p. 930.
 - 3) N. Hatta, H. Takuda, R. Ishii and H. Fujimoto: *ISIJ International*, 29 (1989), p. 605.
 - 4) N. Hatta, H. Fujimoto, R. Ishii, Y. Umeda and J. Kokado: *ISIJ International*, 29 (1989), p. 911.
 - 5) F. E. Marble: *Ann. Rev. Fluid Mech.*, 2 (1970), p. 397.
 - 6) S. Osher and S. R. Chakravarthy: *J. Comp. Phys.*, 50 (1983), p. 447.
 - 7) S. R. Chakravarthy and S. Osher: *A. I. A. A. J.*, 21 (1983), p. 1241.
 - 8) S. R. Chakravarthy and S. Osher: *A. I. A. A. Paper 85-0363*.
 - 9) P. L. Roe: *J. Comp. Phys.*, 43 (1981), p. 357.
 - 10) S. R. Chakravarthy: *A. I. A. A. Paper 86-0243*.
 - 11) K. Sawada, E. Shima and T. Matsuda: *Mem. Fac. Eng. Kyoto Univ.*, 51 (1989), p. 124.
 - 12) T. Matsuda, Y. Umeda, R. Ishii, A. Yasuda and K. Sawada: *Mem. Fac. Eng. Kyoto Univ.*, 49 (1987), p. 84.
 - 13) A. Powell: *Proc. Phys. Soc.*, B 66 (1953), p. 1039.
 - 14) R. Ishii and Y. Umeda: *Phys. Fluids*, 30 (1987), p. 752.
 - 15) E. S. Love, C. E. Grigsby, L. P. Lee and W. W. Roberts: *NASA Technical Report R-6*, 1959.
 - 16) N. Kobayashi, T. Nakagawa and M. Nishida: *Proc. Intl. Symp. of RGD (ed. H. Oguchi)*, Tokyo Univ., 1984.
 - 17) O. M. Belotserkovskii: *J. Appl. Math. Mech.*, 24 (1960), p. 744.
 - 18) A. Powell: *J. Acoust. Soc. Am.*, 83 (1988), p. 515.
 - 19) R. Ishii, N. Hatta, Y. Umeda and M. Yuhi: to be published in *J. Fluid Mech.*
 - 20) N. Hatta and M. Nakamura: *ISIJ International*, 29 (1989), p. 796.
 - 21) C. B. Henderson: *A. I. A. A. J.*, 14 (1976), p. 259.
 - 22) D. J. Carlson and R. F. Hoglund: *A. I. A. A. J.*, 2 (1964), p. 1980.